J. Fluid Mech. (2007), *vol.* 570, *pp.* 307–346.
doi:10.1017/S0022112006002771 Printed in the United Kingdom

Statistical structure of turbulent-boundary-layer velocity–vorticity products at high and low Reynolds numbers

By P. J. A. PRIYADARSHANA[1]†, J. C. KLEWICKI[1]‡, S. TREAT[2] AND J. F. FOSS[2]

[1]Department of Mechanical Engineering, University of Utah, Salt Lake City, UT 84112, USA
[2]Department of Mechanical Engineering, Michigan State University, East Lansing, MI 48824, USA

(Received 8 August 2005 and in revised form 12 June 2006)

The mean wall-normal gradients of the Reynolds shear stress and the turbulent kinetic energy have direct connections to the transport mechanisms of turbulent-boundary-layer flow. According to the Stokes–Helmholtz decomposition, these gradients can be expressed in terms of velocity–vorticity products. Physical experiments were conducted to explore the statistical properties of some of the relevant velocity–vorticity products. The high-Reynolds-number data ($R_\theta \simeq O(10^6)$, where θ is the momentum thickness) were acquired in the near neutrally stable atmospheric-surface-layer flow over a salt playa under both smooth- and rough-wall conditions. The low-R_θ data were from a database acquired in a large-scale laboratory facility at $1000 < R_\theta < 5000$. Corresponding to a companion study of the Reynolds stresses (Priyadarshana & Klewicki, *Phys. Fluids*, vol. 16, 2004, p. 4586), comparisons of low- and high-R_θ as well as smooth- and rough-wall boundary-layer results were made at the approximate wall-normal locations $y_p/2$ and $2y_p$, where y_p is the wall-normal location of the peak of the Reynolds shear stress, at each Reynolds number. In this paper, the properties of the $v\omega_z$, $w\omega_y$ and $u\omega_z$ products are analysed through their statistics and cospectra over a three-decade variation in Reynolds number. Here u, v and w are the fluctuating streamwise, wall-normal and spanwise velocity components and ω_y and ω_z are the fluctuating wall-normal and spanwise vorticity components. It is observed that v–ω_z statistics and spectral behaviours exhibit considerable sensitivity to Reynolds number as well as to wall roughness. More broadly, the correlations between the $\boldsymbol{v}$ and $\boldsymbol{\omega}$ fields are seen to arise from a 'scale selection' near the peak in the associated vorticity spectra and, in some cases, near the peak in the associated velocity spectra as well.

1. Introduction

There are numerous important applications involving high-R_θ turbulent-boundary-layer flows; see for example, Gad el Hak & Bandyopadyay (1994) and DeGraaff & Eaton (2000). (Here, R_θ is the Reynolds number based on momentum thickness:

† Present address: Department of Mechanical and Nuclear Engineering, Kansas State University, Manhattan, KS 66506, USA.
‡ Present address: Department of Mechanical Engineering, University of New Hampshire, Durham, NH 03824, USA.

$R_\theta = U_\infty \theta/\nu$, where U_∞ is the free-stream velocity, θ is the momentum-deficit thickness and ν is the kinematic viscosity.) The R_θ values encountered in many such applications, however, are often orders of magnitude higher than those capable of detailed study by computation or by typical laboratory experimentation.

An important effect of increasing Reynolds number is that the outer length and velocity scales (characterized by δ and U_∞) become increasingly large relative to the corresponding inner scales (characterized by the friction velocity U_τ $(=\sqrt{\tau_w/\rho})$ and ν). Here, τ_w and ρ are the wall shear stress and mass density, respectively. Currently, the effects of separation of scales on momentum transport are not well understood. Among others, an important objective of this paper is to explore the effects of scale separation on the mean dynamics. In addition, wall roughness can become significant in high-R_θ turbulent boundary layers (e.g. DeGraaff & Eaton 2000; Priyadarshana & Klewicki 2004*b*). The present study also provides information regarding the effects of wall roughness (over a limited roughness range) on momentum transport at high-R_θ.

There is evidence that the predominant motions participating in turbulent-stress production and transport have strong vortical signatures (Willmarth 1975; Robinson 1991; Smith *et al.* 1991; Falco 1991; Adrian, Meinhart & Tomkins 2000). Some of the wall-layer features having connections to these vortical motions are low-speed streaks, ejections, sweeps and internal shear layers. One can readily show that (*a*) the gradient of the kinematic Reynolds shear stress, $-\overline{uv}$, appears in the mean momentum balance, shown below in (1.1) for a two-dimensional flat-plate turbulent boundary layer in the (x, y)-plane, and that (*b*) this gradient may be expressed as a difference of velocity–vorticity correlations, as shown in (1.4). The latter relationship is a reduction of the tensor identity shown in (1.2) for a well-developed flow (e.g. Hinze 1975; Klewicki 1989*b*) and is also a result of the Stokes–Helmholtz decomposition.

The mean momentum balance for a two-dimensional incompressible statistically stationary flow over a flat plate is given by

$$U\frac{\partial U}{\partial x} + V\frac{\partial U}{\partial y} = \frac{\partial}{\partial y}\left(\nu\frac{\partial U}{\partial y} - \overline{uv}\right). \tag{1.1}$$

The tensor identity

$$\frac{\partial \overline{u_j u_i}}{\partial x_j} = -\epsilon_{ijk}\overline{u_j \omega_k} + \frac{1}{2}\frac{\partial \overline{u_j u_j}}{\partial x_i} \tag{1.2}$$

has relevance to the Reynolds stress-gradient term. That is, when $i = 1$,

$$\frac{\partial \overline{uv}}{\partial y} = \overline{w\omega_y} - \overline{v\omega_z} + \frac{1}{2}\frac{\partial \overline{(v^2 + w^2 - u^2)}}{\partial x}. \tag{1.3}$$

Here x is in the flow direction and y is the wall-normal direction. As is customary, the x and y mean-velocity components are written as U and V, time averaging is denoted by an overbar or an uppercase letter, instantaneous quantities, denoted by a tilde, are defined as the sum of a mean and fluctuation (e.g. $\tilde{u} = U + u$) and vorticity components are identified by their subscript. Inner normalization is denoted by a superscript plus sign. All r.m.s. measures of the fluctuations are represented by a superscript prime.

As originally proposed by Hinze (1975), $\overline{w\omega_y} - \overline{v\omega_z}$ may be thought of as the active or rotational component of the motion, as proposed by Townsend (1961), and the streamwise gradient $(\partial/\partial x)\overline{(v^2 + w^2 - u^2)}$ as the inactive or irrotational component of the motion. Klewicki (1989*a*, *b*) measured this streamwise gradient over the range $1000 \lesssim R_\theta \lesssim 5000$ and found that it was generally about three orders of magnitude

smaller than $\overline{w\omega_y} - \overline{v\omega_z}$. Thus, for a well-developed turbulent boundary layer, the wall-normal Reynolds stress gradient can be well approximated by

$$-\frac{\partial \overline{uv}}{\partial y} \cong \overline{v\omega_z} - \overline{w\omega_y}. \tag{1.4}$$

With (1.3), (1.1) becomes

$$U\frac{\partial U}{\partial x} + V\frac{\partial U}{\partial y} = -\frac{1}{2}\frac{\partial \overline{v^2}}{\partial x} - \frac{1}{2}\frac{\partial \overline{w^2}}{\partial x} + \frac{1}{2}\frac{\partial \overline{u^2}}{\partial x} + \frac{\partial}{\partial y}\left(\nu\frac{\partial U}{\partial y}\right) + \overline{v\omega_z} - \overline{w\omega_y}. \tag{1.5}$$

In this expression, the difference in the velocity–vorticity correlations constitutes the axial component of the Lamb vector (Lele 1992; Wu, Zhou & Wu 1996).

As shown by various authors (Sreenivasan 1989; Wei *et al.* 2005), the wall-normal position of the peak Reynolds stress occurs at $y_p^+ \simeq 2(\delta^+)^{1/2}$ for smooth-wall turbulent boundary layers. Here δ^+ is the Karman number or the inner-normalized boundary-layer thickness. By definition, the wall-normal gradient of the Reynolds shear stress is zero at y_p. Therefore, with regard to affecting a time rate of change of mean momentum, the $-\partial\overline{uv}/\partial y$ term in (1.1) acts as a source for $y < y_p$ and a sink for $y > y_p$. Further insight into this momentum source/sink character is provided by (1.4), showing that $-\partial\overline{uv}/\partial y$ comes about directly through interactions between the velocity and vorticity fields.

For $i = 2$, the identity (1.2) yields

$$\frac{\partial q}{\partial y} = 2\overline{v\frac{\partial v}{\partial y}} - \overline{u\omega_z} + \overline{w\omega_x}. \tag{1.6}$$

Equation (1.6) provides a description of the flow-field interactions that establish the wall-normal gradient of the turbulent kinetic energy, $q = \frac{1}{2}(\overline{u^2 + v^2 + w^2})$. As shown, these are related to the difference in the velocity–vorticity correlations as well.

Independently of the physics embodied in (1.2), it has long been established that a fluctuating vorticity field is one of the important characteristics of turbulent flows. More specifically, vortex stretching has been postulated as the mechanism by which larger eddies transfer angular momentum to smaller eddies and in doing so it also sustains the classically postulated energy cascade. This mechanism is likely to be the underlying reason why most turbulent flows are characterized by high levels of high-frequency vorticity fluctuations (Tennekes & Lumley 1994; Balint, Vukoslavcevic & Wallace 1987). For turbulent wall flows, free-stream kinetic energy is converted to turbulent kinetic energy and dissipated to internal energy. Associated with this (1.4) and (1.6) explicitly indicate that vortical motions, via their interaction with the velocity field, participate in generating turbulent stress gradients. It is also well established that vorticity-field information is highly useful in understanding the organized motions in time-dependent viscous flows (Balint *et al.* 1987, 1991; Wallace & Foss 1995; Honkan & Andreopoulos 1997). Time-resolved measurements of vorticity, however, require a probe with very good spatial and temporal resolution (Wyngaard 1969; Klewicki & Falco 1990; Balint *et al.* 1991; Rajagopalan & Antonia 1993; Wallace & Foss 1995; Folz 1997; Honkan & Andreopoulos 1997). Maintaining good spatial resolution at high-R_θ is an especially acute challenge.

As revealed in (1.4) and (1.6), velocity–vorticity correlations are important in describing wall-normal stress gradients. Relatively few studies, however, have measured or computed data relative to (1.4) and (1.6). Klewicki (1989*b*) provided a significant documentation of velocity–vorticity correlations in turbulent boundary

layers. His results indicate considerable R_θ variations in the $\overline{v\omega_z}^+$ profile but a much smaller relative variation in the $\overline{u\omega_z}^+$ profile over the range $1000 \lesssim R_\theta \lesssim 5000$. Subsequent studies by Ong (1992) and Rovelstad (1991) also present velocity–vorticity correlations. Generally, these are in good agreement with the results of Klewicki (1989*b*) as well as those of Rajagopalan & Antonia (1993). The latter authors studied the structure of the velocity field associated with the spanwise vorticity field in a turbulent boundary layer at $R_\theta = 1450$. They presented correlation coefficients and cross-correlation functions associated with the $v\omega_z$ and $u\omega_z$ products. Crawford & Karniadakis (1997) studied the characteristics of the components of the Lamb vector in channel flows with direct numerical simulation (DNS). The Reynolds number based on channel height in this study was 5000.

Regarding scale-separation effects, the generally accepted properties of the velocity and vorticity fields in turbulent flows indicate that with increasing Reynolds number the spectral peaks in the fluctuating $\boldsymbol{v}$ and $\boldsymbol{\omega}$ fields move to increasingly disparate wavenumbers (e.g. Balint *et al.* 1991). Thus, one possibility is that these interactions occur within a decreasingly narrow, intermediate, wavenumber band (relative to the total span of possible wavenumbers) over which the relevant $\boldsymbol{v}$ and $\boldsymbol{\omega}$ spectral components overlap. Velocity–vorticity cospectra provide some evidence that intermediate scales are important (Priyadarshana & Klewicki 2004*a*). A central objective of the present effort is to explore the interactions leading to $-\partial\overline{uv}/\partial y$ as δ^+ becomes large.

2. Experimental setup and methodology

2.1. *Experimental facility*

The high-R_θ experimental data used in this study were obtained at the Surface Layer Turbulence and Environmental Science Test (SLTEST) facility, as described in Metzger & Klewicki (2001) and Klewicki & Metzger (2004). In particular, a significant number of the velocity–vorticity time series analysed herein were derived from the experiments described by Priyadarshana & Klewicki (2004*b*).

All the measurements at the SLTEST facility were made around sunset, under near neutrally stable atmospheric conditions. The thermal stability of the atmospheric surface layer was assessed using the Monin–Obukov stability parameter $\zeta(\zeta = y/l)$, where y is the wall-normal coordinate. The Monin–Obukov length l is defined as

$$l = -\frac{\Theta_0 U_\tau^3}{\kappa g \overline{\theta v}}, \tag{2.1}$$

where, Θ_0 is the mean temperature of an adiabatic atmosphere, θ is the fluctuating component of the difference between the actual temperature and Θ_0 and $\kappa(=0.41)$ is the von Karman constant. Detailed information on stability criteria is given in Priyadarshana & Klewicki (2004*b*). Experimentally estimated integral parameters utilizing miniSODAR (Metzger, Klewicki, Bradshaw & Sadr 2001; Priyadarshana 2004) velocity profiles for smooth and rough surface flows are summarized in table 1. For more information on wall roughness, refer to Metzger (2002), Klewicki & Metzger (2004) and Metzger & Klewicki (2001). In this table it is interesting to note that the present high-R_θ shape factors agree well with the recent $H(R_\theta)$ prediction of Nagib, Chauhan & Monkewitz (2005). Similarly, the shape factors for the data of Klewicki (1989*a*) at $1010 < R_\theta < 4850$ agree well with their results. The wall-friction velocity U_τ was measured using a 2.4 m diameter drag balance (Sadr & Klewicki 2000). The inner-normalized boundary-layer parameters, the wall-roughness values k_s^+ and the

R_θ	U_∞ (m s^{-1})	θ (m)	δ^* (m)	δ (m)	H
$\backsim 2\times10^6$	6.31	5.39	6.47	84	1.19
$\backsim 4\times10^6$	17.2	4.43	5.27	69	1.24
$\backsim 2\times10^6$	7.35	4.57	5.58	67	1.22
1010	0.607	0.0248	0.0360	0.206	1.45
2870	1.752	0.0245	0.0343	0.205	1.40
4850	2.981	0.0243	0.0335	0.199	1.38

TABLE 1. Estimated integral parameters for the high- and low-R_θ boundary layers. Note that the values cited for the high-R_θ experiments are typical, but varied within the ensemble of acquisition runs collected. Here δ^* is the displacement thickness, δ is the boundary-layer thickness and H is the shape factor. All the other symbols are as explained in the main text.

R_θ	U_τ (m s^{-1})	ν (m^2 s^{-1})	k_s^+	δ^+	y_p (m)	y_p^+
$\backsim 2\times10^6$	0.1962	1.85×10^{-5}	$25\sim50$	8.9×10^5	0.1783	1892
$\backsim 4\times10^6$	0.5366	1.85×10^{-5}	≈300	2.0×10^6	0.0976	2825
$\backsim 2\times10^6$	0.2803	1.87×10^{-5}	≈500	1.01×10^6	0.1335	2010
1010	0.0282	1.5×10^{-5}	smooth	388	2.58×10^{-2}	39.4
2870	0.0707	1.5×10^{-5}	smooth	966	1.63×10^{-2}	62.2
4850	0.1125	1.5×10^{-5}	smooth	1493	1.27×10^{-2}	77.3

TABLE 2. Inner-normalized wall-roughness values k_s^+, inner parameters and estimated peak locations y_p of $-\overline{uv}^+$ for high- and low-R_θ smooth- and rough-wall turbulent boundary layers. y_p^+ is the inner normalized peak position of the Reynolds stress.

estimated inner-normalized peak-Reynolds-stress locations at each R_θ are shown in table 2.

To assess the R_θ effects, the highest-R_θ data were compared with well-resolved velocity and vorticity measurements of Klewicki (1989*a*), Klewicki & Falco (1990, 1996) and Klewicki, Murray & Falco (1994). Some previously unreported results from the data sets of Klewicki (1989*a*) relating to the statistics and spectra are also presented herein.

2.2. *Instrumentation and data acquisition*

Three types of custom-made hot-wire probes were used to acquire the streamwise, wall-normal and spanwise velocity components. The first probe used by the University of Utah group was the six-element x-array probe (6X probe) described in Priyadarshana & Klewicki (2004*b*). This probe, composed of three x-arrays, was used to acquire instantaneous streamwise and wall-normal velocity components at three closely spaced wall-normal positions. The second probe used by the University of Utah group was a custom-made six-element v-array sensor (6V probe). In this probe, the six wires were arranged in a four v-array configuration facilitating the measurement of instantaneous streamwise and spanwise velocity components at two different wall-normal locations and two different spanwise locations. The vorticity probes, utilized in the present study by the Michigan State University group, were formed from arrays of four hot-wires. In this configuration, two hot-wires are parallel to one another and perpendicular to the probe body while the other two wires cross to form an X as viewed from a vantage point along the axis of one of the parallel wires (Wallace & Foss 1995). This array of sensors provides a microcirculation domain of

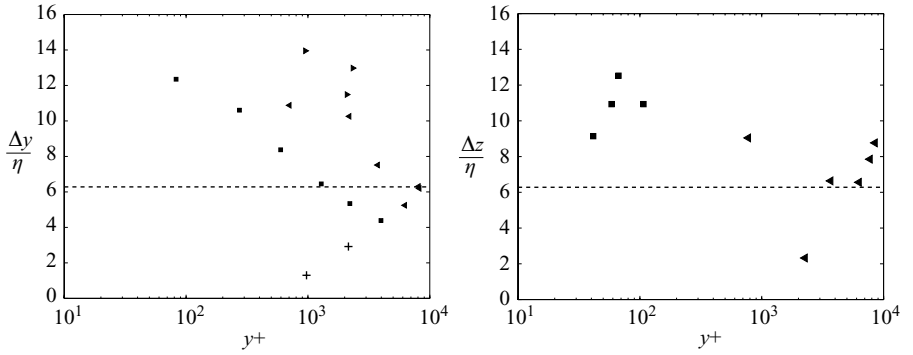

FIGURE 1. (*a*) Six-element x-array sensor wire separation Δy and (*b*) six-element v-array sensor wire separation Δz normalized by the Kolmogorov length η, as a function of y^+. ■, $R_\theta = 2 \times 10^6$, $k_s^+ \approx 25 \sim 50$; ►, $R_\theta = 4 \times 10^6$, $k_s^+ \approx 300$, rough-wall; ◄, $R_\theta = 2 \times 10^6$, $k_s^+ \approx 500$, rough-wall; — — —, $\Delta y/\eta = 2\pi$ or $\Delta z/\eta = 2\pi$, the optimal probe resolution suggested by Folz (1997).

order 1 mm^2. Previous measurements using this probe are described in Foss (1994) and Morris & Foss (2004).

The Wheatstone-bridge circuits for both six-element hot-wire probes were provided by A.A. Lab-Systems AN-1003 constant-temperature hot-wire anemometers. The six-wire signals were digitized at a sampling frequency of 5 kHz using 16-bit simultaneous sample- and -hold analog-to-digital converters. Details relating to the calibration and operating procedures of the six-wire probes are given in Priyadarshana & Klewicki (2004*b*). The four-sensor vorticity probes were driven by a 16-channel pulse-width-modulated constant-temperature anemometer (PWM-CTA). The operating principle for this anemometer is described in detail in Foss, Bohl & Hicks (1996). The data samples for these probes were collected at a rate of 50 kHz. The reasons for this very high sampling rate pertain to the microcirculation-based vorticity-estimation methodology described in § 2.4.2 below. The calibration and operating procedures for these sensors are given in Treat (2006).

All the hot-wire sensors employed 5 μm diameter tungsten wires. These wires had a sensor length of 1 mm, which is 10–15 wall units at $R_\theta \simeq 2 \times 10^6$. This is also the nominal Δy^+ spacing in the four-wire probes, which was between 1.3η and 3.0η. Here η is the Kolmogorov length scale; $\eta = (\nu^3/\epsilon)^{1/4}$ where ϵ is the dissipation and ν is the kinematic viscosity. (The dissipation in the log-law region was estimated by employing the assumption that the turbulent kinetic energy production equals the dissipation for the Utah group measurements and by using $\eta = 15\nu\overline{u}^2/\lambda_u^2$, where λ_u is the Taylor microscale based on u for the Michigan State University group measurements). The inner-normalized wall-normal spacing Δy^+ between adjacent x-arrays in the six-element x-array probe, however, was generally around 30 wall units. As shown in figure 1(*a*), the Δy range for this probe was between 4η and 15η in the log-law region. Similarly, the inner-normalized spanwise spacing Δz^+ between two v-arrays in the six-element v-array probe was around 30 wall units. This was between 2η and 13η, as shown in figure 1(*b*). According to Folz (1997), for atmospheric measurements a Δy value of about $2\pi\eta$ yields minimal attenuation of the important scales contributing to vorticity. He also showed that at this Δy value, the effect of the instrument noise in the AN1003 system ($1 \sim 2$ mV) is greatly attenuated. This optimal probe resolution is depicted by the horizontal dashed line in figure 1. As indicated, some high-R_θ six-wire

probe data fall above this line. Thus, some attenuation of the high-R_θ ω_z signals is expected. The present four-wire probe data show minimal attenuation.

2.3. *Data-analysis techniques*

2.3.1. *Techniques used in computing turbulent statistics*

A primary quality measure of the instantaneous signals of six-wire probes selected for the analysis was that during acquisition the wind did not exhibit transient (ramp up, ramp down) behaviour. Thus, only the time series of velocity and vorticity that, when plotted, exhibited a well-defined horizontal mean line were selected for subsequent analysis (Priyadarshana & Klewicki 2004*b*). All the turbulence quantities for six-wire probes were obtained by subtracting the overall mean of each individual signal. In this methodology, changes in the local mean velocity within different runs were not considered as a part of the low-frequency turbulence but as a change in the mean velocity. In interpreting results derived in this way, particular attention was paid to spectra and cospectra for the possible influences of low-wave-number truncation. The present four-wire data, from two days, indicated gradually decreasing mean velocities during the acquisition period. A linear relationship such that the most accurate streamwise velocity fluctuations could be defined was used to express these gradual decreases. In the present study, 30–40 minute observation times (and often more) at each point were used to compute the flow statistics.

2.4. *Extraction of vorticity time series*

2.4.1. *Extraction of vorticity time series from the six-wire probes*

For the six-wire probes, the wall-normal velocity gradient $\partial u/\partial y$ (one contribution to $\omega_z = \partial v/\partial x - \partial u/\partial y$) was obtained directly by differencing the u-components from the top and the middle x-arrays of the six-element x-array probe. Similarly, the spanwise velocity gradient $\partial u/\partial z$ (a contribution to $\omega_y = \partial u/\partial z - \partial w/\partial x$) was obtained directly by differencing the u-components from the left and the right v-arrays of the six-element v-array probe. The streamwise gradients $\partial v/\partial x$ and $\partial w/\partial x$ were computed using Taylor's hypothesis. A local mean streamwise velocity computed over 6000 viscous time units was used as the convection velocity in Taylor's hypothesis for all the six-wire-probe data.

2.4.2. *Extraction of vorticity time series from the four-wire probes*

The computational strategy of extracting the transverse vorticity from the four-sensor probe is given in Wallace & Foss (1995). Briefly stated, a microcirculation domain (of area $\delta s \times \delta n$) is created where the domain is oriented in the locally defined streamwise (s) direction with a height δn equal to the separation between the two straight wires δy. The centre point of the domain is established at time, t_k. Convected steps

$$\pm\delta s_{krtk} = \pm\left(\frac{V_1 + V_2}{2}\right)_{k\pm\delta k} \cos(\gamma_{k+t\delta k} - \langle\gamma\rangle) \tag{2.2}$$

'build' the microdomain by adding segments to δs until $\delta s \geqslant \delta n$. $\langle\gamma\rangle$ is the cumulative orientation angle of the domain centreline and V_1, V_2 are the velocity magnitudes from the straight wires.

The circulation Γ around this domain is formally equal to the spatially averaged transverse ($\perp$) vorticity within the domain as

$$\omega_\perp = \frac{1}{\delta s \delta n} \int \boldsymbol{V} \cdot \mathrm{d}\boldsymbol{l} \tag{2.3}$$

The velocity–length segments are obtained for each time step. This underlies the requirement for a very high sampling rate at the given flow speeds. In the overall computation, the velocity magnitudes $V_{1,2}\cos(\gamma_{k\gamma\delta k}-\langle\gamma\rangle)$ contribute to the s-segments, and the $V\sin(\gamma-\langle\gamma'\rangle)$ values at the 'ends' of the microdomain also contribute to the microcirculation.

2.4.3. *Techniques used in computing event durations*

Event-duration analyses were performed to obtain the vorticity time scales. These analyses were similar to those performed by Klewicki, Falco & Foss (1992) and Klewicki & Falco (1996). The magnitudes of the fluctuating vorticity signals were tracked from the beginning to the end of the signal. When these magnitudes exceeded a specified threshold level (positive or negative), counting of an event duration was initiated. The event continued until its magnitude dropped below the threshold. Furthermore, to account for small-amplitude deviations that might prematurely end events, and to maintain consistency with the event-duration analyses of Klewicki *et al.* (1992) and Klewicki & Falco (1996), the present method required the signal to drop 20% below the threshold before an event was terminated. The threshold for the present analyses was selected as 1.0 r.m.s. (e.g. $1.0\omega_z'$).

2.4.4. *Spectral analysis*

The process used to compute the cospectra and power spectra was the same as that described by Priyadarshana & Klewicki (2004*b*). Briefly, the signal was divided into windows of 4096 data points each before computation of the fast Fourier transform (FFT). The power spectral density and the cross spectral density were computed using Welch's averaged modified-periodogram method. A Hanning window of the same size as the signal-window size was used to minimize the spectral leakage and the signal was overlapped by 50% to improve averaging. Similarly to the method used by Saddoughi & Veeravalli (1994), the low-frequency portion of the spectrum was obtained by down-sampling the signals using an anti-aliasing (low-pass) finite-duration impulse-response (FIR) filter. The cospectra of velocity and vorticity were obtained using the real part of the cross spectral density (Bendat & Piersol 1986; Shiavi 1999).

3. Results

Detailed results are presented and explained in this section. It is relevant to examine the statistical properties of the individual velocity and vorticity signals prior to an analysis of the velocity–vorticity products. Section 3.1 describes the statistics for the velocity components and § 3.2 describes spanwise vorticity component statistics. Section 3.3 describes vorticity time scales. Analyses of the velocity–vorticity correlations $v\omega_z$, $w\omega_y$ and $u\omega_z$ are then presented in §§ 3.4, 3.5 and 3.6, respectively. These include statistics and spectral analysis.

3.1. *Velocity component statistics*

3.1.1. *Mean streamwise velocity profiles*

The mean streamwise velocities acquired during near neutral conditions are shown in figure 2. The abscissa is the logarithm of the inner-normalized wall-normal distance, $y^+(=yU_\tau/\nu)$, and the ordinate is the inner-normalized mean velocity, $U^+(=U/U_\tau)$. The data close to the wall, shown in dark symbols, were acquired using the six-wire probes. The data between 60 m and 100 m ($y^+\simeq 2\times10^5$ to $y^+\simeq 1\times10^6$) were

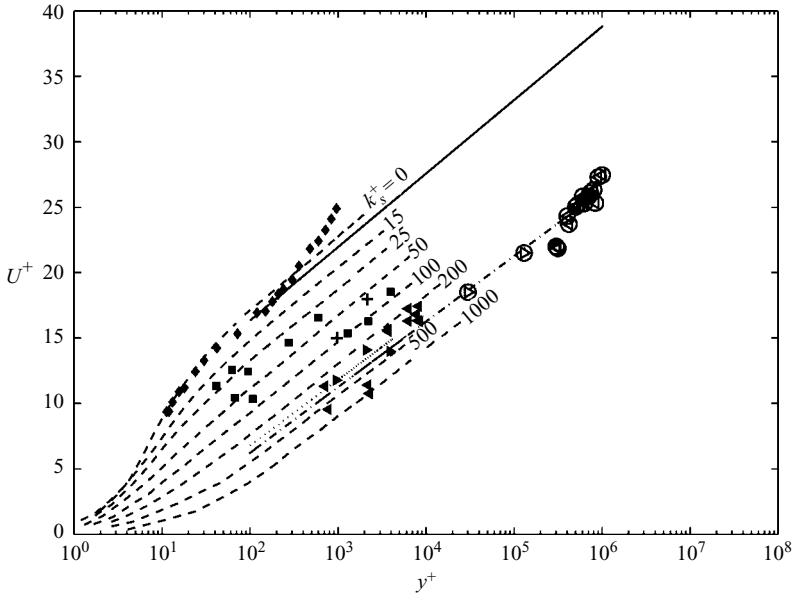

FIGURE 2. Inner-normalized mean-velocity profiles U^+ vs. y^+ at various k_s^+ values, for the atmospheric surface layer during near neutral stability: $- \cdot - \cdot -$, $U^+ = (1/0.39) \ln y^+ - 3.79$; $\cdots$, $U^+ = (1/0.46) \ln y^+ - 3.29$; ——, $U^+ = (1/0.41) \ln y^+ + 5.1$. The other symbols are defined in table 3. The representative low-R_θ smooth-wall profile is from Klewicki & Falco (1990).

acquired using the miniSODAR. The three-dimensional sonic anemometers were used to acquire velocities at intermediate heights from 1 m to 5 m ($y^+ \simeq 2 \times 10^4$ to $y^+ \simeq 2 \times 10^5$). Each hot-wire data point shown in figure 2 represents a 30–40 minute time average. The sonic anemometer data and the miniSODAR data, simultaneously acquired at much greater elevations above the ground, show striking agreement with the logarithmic trend of the near-wall hot-wire data. Furthermore, the logarithmic curve-fits between the hot-wire, the miniSODAR and sonic-anemometer data show that the mean-velocity gradient is in good agreement with a von Karman constant κ of about 0.4. This indicates a strong mechanical coupling of the atmospheric surface layer (ASL) to the surface condition up to y^+ values near 10^6, and thus provides evidence that, for this statistic, the near neutrally stable ASL behaves quite similarly to a canonical zero-pressure-gradient turbulent boundary layer.

The wall roughness was estimated in terms of the equivalent sand roughness k_s, using the correlation with the downward shift in the mean-velocity profile of Krogstad, Antonia & Browne (1992):

$$\Delta \overline{U}^+ = \frac{1}{\kappa} \ln k_s^+ - 3.2. \tag{3.1}$$

The data in figure 2 shown by squares (■) were taken during summer 1999 and summer 2004 when the salt playa was relatively smooth. For these data, the downward shift is minimal and the inner-normalized wall roughness k_s^+ for the first five data points is around 25 and the same quantity for the next five data points is between 50 and 100. The next set of data, shown by forward triangles (►), was taken during summer 2000 when the salt playa was relatively rough as a result of drier weather. The downward shift for these data is significantly greater, yielding a k_s^+ estimate of about 300. The data shown by backward triangles (◄) were taken during summer 2001. In

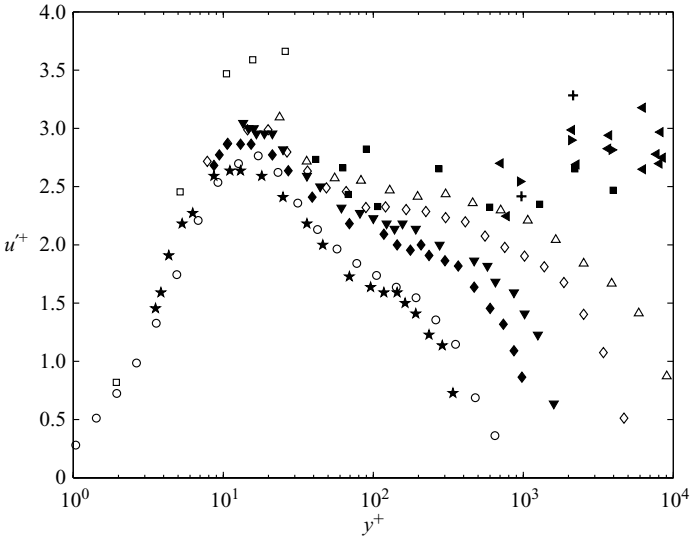

FIGURE 3. The present high-R_θ inner-normalized streamwise velocity-intensity profiles with, for comparison, selected well-resolved low-R_θ data. The symbols are defined in table 3.

this case, the salt playa was rougher than in the year 2000: $k_s^+ \simeq 500$. The data shown by the plus symbols were acquired in summer 2003 using the four-wire probes; then $k_s^+ \simeq 100$. For comparison, the $R_\theta = 2870$ mean-velocity profile from Klewicki (1989*a*) is also presented.

3.1.2. *Streamwise velocity intensities*

Figure 3 shows the intensities of the inner-normalized streamwise velocity fluctuations for the present high-R_θ relatively-smooth-wall ($k_s^+ \approx 25 \sim 50$) and rough-wall ($100 \lesssim k_s^+ \lesssim 500$) turbulent boundary layers. The abscissa is the inner-normalized wall-normal distance y^+ and the ordinate is the inner-normalized streamwise intensity, $u'^+ (\equiv u'/U_\tau)$. A key to the symbols is given in table 3 along with estimates of R_θ and k_s^+. For comparison, smooth-wall turbulent-boundary-layer streamwise intensities from Klewicki (1989*a*), DeGraaff & Eaton (2000) and Metzger & Klewicki (2001) are shown as well. For the high-R_θ flow, note that the boundary-layer thickness is approximately 1×10^6 wall units. Thus, all the present high-R_θ data fall well within the logarithmic layer. As can be seen in figure 3, there is a significant dependence of u'^+ on R_θ. At greater y^+, this expected behaviour can clearly be seen in the larger u'^+ values of the present high-R_θ data. There is also good agreement between the data from the six-element and four-element hot-wire probes. The present high-R_θ u'^+ results for $k_s^+ \gtrsim 300$ may also indicate a slight surface roughness effect, as u'^+ appears to increase slightly with increasing wall roughness. This is observed well above the roughness sublayer ($3 \sim 5$ roughness heights). This result, however, requires further investigation. Regarding this issue, Krogstad *et al.* (1992) and Flack, Schultz & Shapiro (2005) observed no significant change in the streamwise intensity in rough-wall turbulent boundary layers outside the roughness sublayer. In any case, it is apparent that the effects of surface roughness on the streamwise intensity are small compared with the effects of the Reynolds number.

Symbol	Source	Data type	Probe	R_θ	k_s^+	l^+	Δy^+
■	present (hot-wire)	ASL	6X and 6V	$\sim 2\times10^6$	25∼50	10	31
►	present (hot-wire)	ASL	6X and 6V	$\sim 4\times10^6$	300	25	66
⧐	present (sonic)	ASL	sonic	$\sim 4\times10^6$	300	—	—
◄	present (hot-wire)	ASL	6X and 6V	$\sim 2\times10^6$	500	16	48
◁	present (miniSODAR)	ASL	SODAR	$\sim 2\times10^6$	500	—	—
+	present (hot-wire)	ASL	four-wire	$\sim 4\times10^6$	100	11.0	11.0
★	Klewicki (1989*a*)	WTBL	(x-wire	1010	smooth	2.0	2.0
◆	Klewicki (1989*a*)	WTBL	and	2870	smooth	4.8	4.8
▼	Klewicki (1989*a*)	WTBL	parallel)	4850	smooth	7.8	7.8
○	DeGraaff & Eaton (2000)	WTBL	LDV	1430	smooth	0.6	—
◇	DeGraaff & Eaton (2000)	WTBL	LDV	13000	smooth	4.4	—
△	DeGraaff & Eaton (2000)	WTBL	LDV	31000	smooth	9.9	—
□	Metzger & Klewicki (2001)	ASL	u-rake	$\sim 5\times10^6$	smooth	9.0	2∼9
⊞	Metzger (2002)	ASL	dual x	$\sim 5\times10^6$	smooth	20	50
◁	Balint *et al.* (1991)	WTBL	nine-wire	2685	smooth	10.9	10.9
▷	Honkan & Andreopoulos (1997)	WTBL	12-wire	2790	smooth	6	10
▽	Rajagopalan & Antonia (1993)	WTBL	four-wire	1450	smooth	13	17
⊕	Spalart (1988)	WTBL	DNS	670	smooth	—	—
⊗	Spalart (1988)	WTBL	DNS	1410	smooth	—	—
✻	Warnack (in Fernholz & Finley 1996)	WTBL	x-array	864	smooth	12	—
×	Warnack (in Fernholz & Finley 1996)	WTBL	x-array	2552	smooth	15	—
⊙	Warnack (in Fernholz & Finley 1996)	WTBL	x-array	4736	smooth	14	—
⊠	Folz (1997)	ASL	u-rake	$\sim 1\times10^6$	smooth‡	6,14	4∼13
—	Crawford & Karniadakis (1997)	CF	DNS	5000‖	smooth	—	—
⊡	Ong (1992)	WTBL	nine-wire	1070	smooth	11.0	≈ 7

‡ transitionally smooth ‖ Reynolds number based on channel height

TABLE 3. Detailed description of flow parameters for the data presented in figures 3–28. ASL: atmospheric surface layer/SLTEST. WTBL: wind tunnel boundary layer. CF: channel flow.

3.1.3. *Wall-normal velocity intensities*

The intensities of the inner-normalized wall-normal velocity fluctuations v'^+ for the present high-R_θ turbulent-boundary-layer flows are shown in figure 4. As noted by DeGraaff & Eaton (2000), v'^+ measurements in turbulent boundary layers are relatively scarce in comparison with u'^+ measurements. DeGraaff & Eaton (2000) presented well-resolved (less than 10 viscous units) laser-Doppler velocimetry (LDV) measurements of the wall-normal stress $\overline{v^2}^+$ for R_θ values ranging from 1430 to 31 000. Fernholz & Finley (1996) compiled the available x-array hot-wire measurements of v'^+. The spatial resolution of these data, however, varies between about 7 and 70 viscous units. The profiles of v'^+ from Klewicki (1989*a*) and DeGraaff & Eaton (2000) are presented for comparison in figure 4. The $R_\theta = 2870$ and 4850 data of Klewicki (1989*a*) in figure 4 exhibit a small but discernible R_θ-dependence, specifically relating to the position of the peak value attained. The value of this plateau, according to DeGraaff & Eaton (2000), is around 1.16. The data at $R_\theta = 1010$, however, show a significant R_θ-dependence. This could be a very-low-R_θ effect, as described by DeGraaff & Eaton (2000). Above R_θ values greater than about 1500, the peak value of v'^+ exhibits very little increase with increasing R_θ. As shown, the low-R_θ ($2000 \lesssim R_\theta \lesssim 31\,000$) v'^+ data have peaks between 1.1∼1.2. Interestingly, the present relatively smooth $R_\theta \simeq 2\times10^6$ data also yield peak values around 1.1∼1.2, the profile

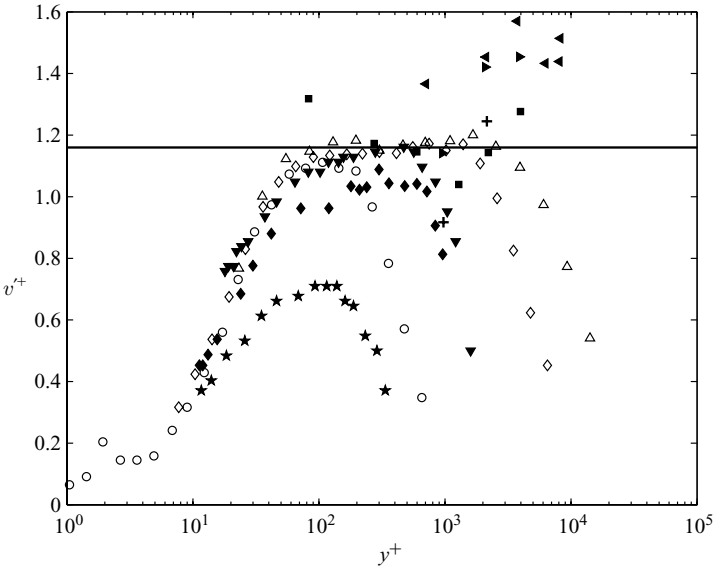

FIGURE 4. The present high-R_θ inner-normalized wall-normal velocity-intensity profiles with, for comparison, selected well-resolved low-R_θ data. The symbols are defined in table 3. The horizontal line corresponds to $v'^+ = 1.16$.

remaining essentially constant with increasing y^+. Therefore, there appears to be very little R_θ-dependence in v'^+ for R_θ values above the low-R_θ regime.

The present high-R_θ rough-wall v'^+ data, however, exhibit noticeably larger magnitudes than the smooth-wall data. The average peak magnitude of these data is about 1.4 for the $k_s^+ \approx 500$ case and about 1.3 for the $k_s^+ \approx 300$ case. One of the present four-wire data points at $k_s^+ \approx 100$ shows $v'^+ \approx 1.2$. These measurements were observed well above 3∼5 roughness heights and thus are in agreement with Krogstad *et al.* (1992), who observed effects of surface roughness in v'^+ well above the roughness sublayer. They are not, however, in agreement with the conclusion of Flack *et al.* (2005), who found little roughness effect in v'^+ above the roughness sublayer. Overall, the present results indicate that v'^+ does not depend significantly on R_θ (for $R_\theta \gtrsim 2000$) but does exhibit a discernible dependence on surface roughness for the k_s^+ and y^+ values explored.

3.1.4. *Spanwise velocity intensities*

Inner-normalized spanwise velocity intensities w'^+ are shown in figure 5. Similarly to the existing low-R_θ results, all the present high-R_θ w'^+ values are greater than the v'^+ values at the same y^+, but less than the corresponding u'^+ values (Honkan & Andreopoulos 1997). The present relatively-smooth-wall data, in relation to the low-R_θ data, show a detectable increase in w'^+ (despite scatter) in the region $40 < y^+ < 110$, exhibiting an average value of approximately 2.06. The average value of w'^+ in the region $700 < y^+ < 10\,000$ is 2.25. The present $R_\theta \simeq 4 \times 10^6$ four-wire data with $k_s^+ \approx 100$ at $y^+ \approx 2000$ agree well with these data. The four-wire data point at $y^+ \approx 973$, however, shows a significantly lower intensity level. The DNS w'^+ results of Spalart (1988) at $R_\theta = 670$ and 1410 and the hot-wire data of Warnack (reported by Fernholz & Finley 1996) are shown for comparison. The data of Warnack at $R_\theta = 4736$ are lower than those of Spalart (1988) at $R_\theta = 1410$; this could be a spatial-resolution effect. The data of Balint *et al.* (1991) at $R_\theta = 2685$ show good agreement with the data of Warnack at $R_\theta = 2552$. In contrast, the data of Honkan & Andreopoulos (1997) show significantly

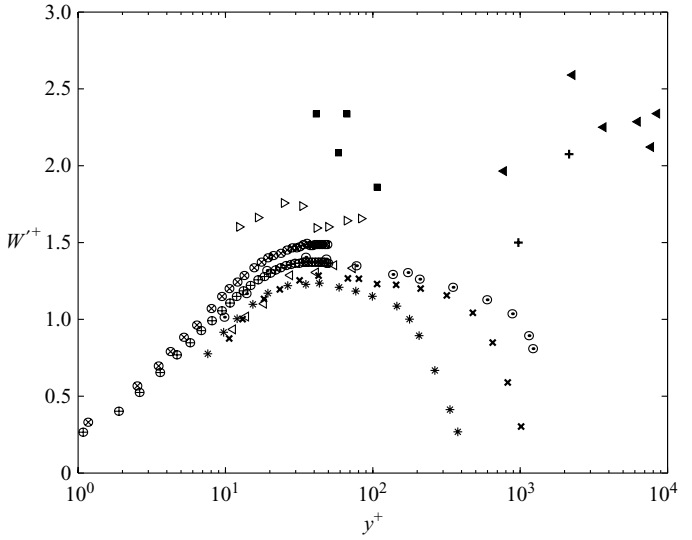

FIGURE 5. The present high-R_θ inner-normalized spanwise-velocity intensity profiles with, for comparison, selected well-resolved low-R_θ data. The symbols are defined in table 3.

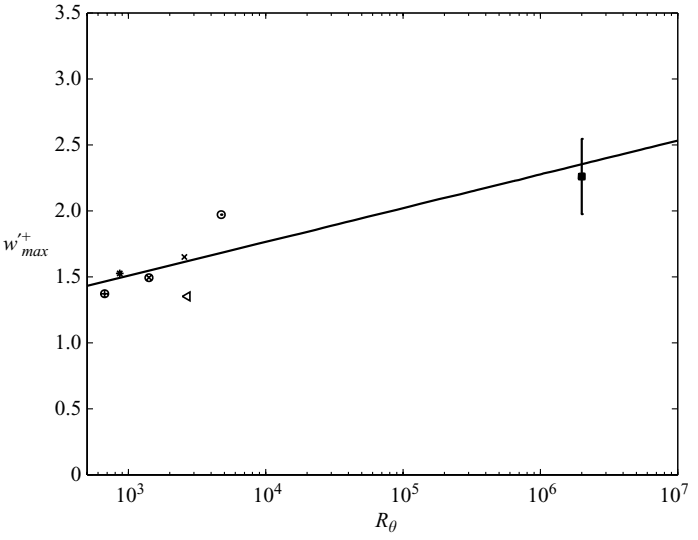

FIGURE 6. Variation of w'^+_{max} vs. R_θ: $w' = 0.256 \log R_\theta + 0.742$ describes the curve-fit. The error bar indicates the total data scatter.

higher values at $R_\theta = 2790$. There is a mild R_θ effect in the data of Warnack, which increases with increasing R_θ for the range $864 < R_\theta < 4736$. In this regard, it is relevant to note that the relative effects of attenuation due to spatial resolution in the data of Warnack are likely to be nearly constant since for these data the wire length only varied between 12 and 15 viscous units. Similarly, the DNS data of Spalart (1988) for $300 < R_\theta < 1410$ show a mild R_θ-dependence. Over the full R_θ range depicted in figure 5, the peak w'^+ data show a significant variation in magnitude.

The peak values of w'^+ from the above data were compiled and plotted as a function of R_θ and are shown in figure 6. The peak w'^+ value exhibits an approximately logarithmic increase with increasing R_θ. The curve-fit shown utilized the entire range

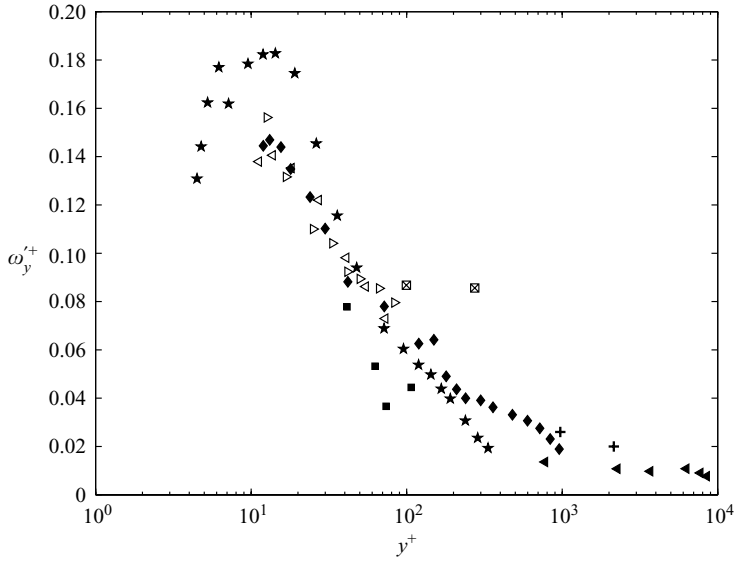

FIGURE 7. The present high-R_θ inner-normalized wall-normal-vorticity intensity profiles with, for comparison, selected well-resolved low-R_θ data: ⋆, $(\partial u/\partial z)'^+$ at $R_\theta = 1010$; ◆, $(\partial u/\partial z)'^+$ at $R_\theta = 2870$. The other symbols represent $\omega_y'^+$ as defined in table 3.

of R_θ. As is evident, there is scatter in the low-R_θ data, although the increasing trend is apparent. The approximately logarithmic increase in w'^+ and u'^+ (DeGraaff & Eaton 2000; Metzger *et al.* 2001), coupled with the noted R_θ-insensitivity of v'^+, is consistent with Townsend's attached-eddy hypothesis (Townsend 1976; Perry & Chong 1982; Perry & Marusic 1995; Marusic, Uddin & Perry 1997).

3.2. *Vorticity-component intensities*

Inner-normalized intensities of the wall-normal and spanwise vorticity fluctuations for the present high-R_θ data are presented in this section. These are compared with well-resolved low-R_θ vorticity-intensity data.

3.2.1. *Wall-normal vorticity intensities*

Inner-normalized intensities of the wall-normal vorticity fluctuations $\omega_y'^+$ are shown in figure 7. As mentioned previously, the rough-wall data were acquired within the range $700 < y^+ < 10^4$ and the relatively-smooth-wall data were acquired within the range $30 < y^+ < 100$. The previous $\omega_y'^+$ data of Honkan & Andreopoulos (1997) at $R_\theta = 2790$ and those of Balint *et al.* (1991) at $R_\theta = 2685$ as well as the previously unpublished $(\partial u/\partial z)'^+$ data of Klewicki (1989*a*) at $R_\theta = 1010$ and 2870 are also shown for comparison. The present relatively-smooth-wall data show slightly lower magnitudes in comparison with the data of Honkan & Andreopoulos (1997) as well as with the data of Balint *et al.* (1991). The $(\partial u/\partial z)'^+$ data of Klewicki (1989*a*) at $R_\theta = 2870$ show very good agreement with the $\omega_y'^+$ data of Honkan & Andreopoulos (1997) and those of Balint *et al.* (1991). The data of Folz (1997) taken at the SLTEST site at $R_\theta \simeq 1 \times 10^6$ are also shown (however, the thermal stability was not systematically quantified during these measurements). These data show significantly higher values in comparison with the present data at $R_\theta \simeq 2 \times 10^6$. The present near-wall relatively-smooth-wall $\omega_y'^+$ data, however, show evidence of melding with the present six-wire and four-wire rough-wall data away from the wall. Overall, the

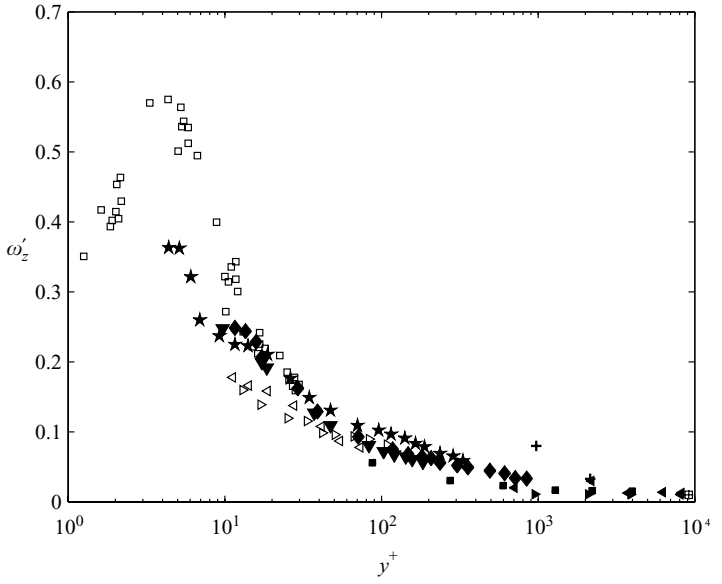

FIGURE 8. The present high-R_θ inner-normalized spanwise-vorticity intensity profiles with, for comparison, selected well-resolved low-R_θ data. The symbols are defined in table 3.

results in figure 7 are taken as evidence that inner normalization constitutes the appropriate scaling for ω_y' (for the y^+ and k_s^+ values explored).

3.2.2. *Spanwise-vorticity intensities*

The present inner-normalized spanwise-vorticity intensities are shown in figure 8 with, for comparison, the available $\omega_z'^+$ data. The previously acquired $\omega_z'^+$ data are given in Balint *et al.* (1991), Wallace & Foss (1995), Klewicki & Falco (1996), Honkan & Andreopoulos (1997) and Metzger & Klewicki (2001). A number of these studies indicate that inner normalization is appropriate while others (e.g. Adrian, Meinhart & Tomkins 2000) have suggested outer normalization. Spalart (1988) explored a mixed scaling.

As can be seen in figure 8, the present high-R_θ smooth- and rough-wall $\omega_z'^+$ data within the log-law region agree quite well with previous low-R_θ data, as well as the high-R_θ data of Metzger (2002). In contrast, the near-wall high-R_θ results of Metzger & Klewicki (2001) show significantly larger values near the edge of the sublayer. Close examination of the present data in figure 8 indicates some evidence of attenuation of $\omega_z'^+$ for $y^+ \lesssim 1000$. As discussed in relation to figure 1(*a*), this is likely to be due to the diminished spatial resolution of the sensor. Overall, there is no apparent effect of surface roughness on the present $\omega_z'^+$ results nor any apparent R_θ effect on $\omega_z'^+$ outside the region near the edge of the viscous sublayer.

3.3. *Vorticity time scales*

Mixing-length arguments often invoke the idea that the size of the eddies participating in the generation of $\overline{uv}$ undergoes a proportional increase with distance from the wall (Prandtl 1925). Previous high-R_θ measurements indicate that the motions contributing to $\overline{uv}$ increase in size with increasing R_θ at a rate less than the rate of increase of δ^+ (Priyadarshana & Klewicki 2004*b*). As shown in (1.4), however, the wall-normal gradient of $\overline{uv}$ can be expressed in terms of velocity–vorticity products. It is, therefore, of interest to characterize the variation in the scales of the ω_y and ω_z motions with

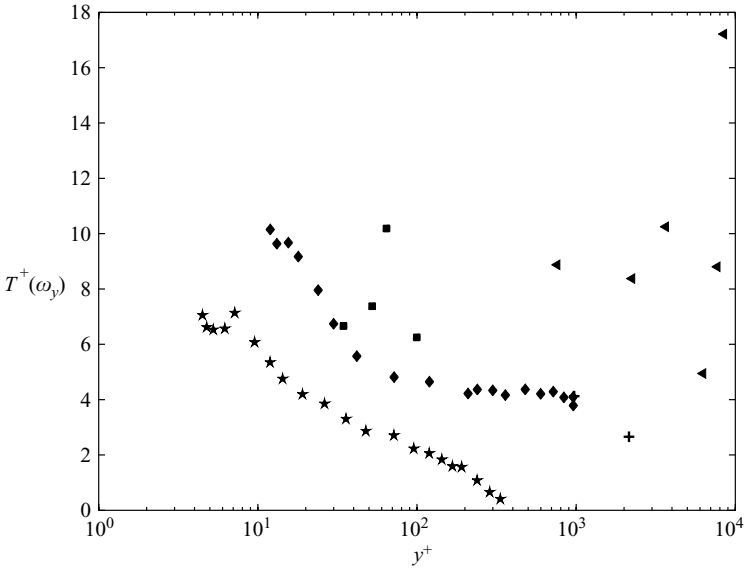

FIGURE 9. Inner-normalized wall-normal-vorticity event durations as a function of y^+: ⋆, $T^+(\partial u/\partial z'^+)$ at $R_\theta = 1010$; ◆, $T^+(\partial u/\partial z'^+)$ at $R_\theta = 2870$. All the other symbols represent $T^+(\omega_y^+)$ as defined in table 3.

increasing wall-normal distance. As described in § 2.4.3, the durations of events above a unit r.m.s. were computed for ω_y and ω_z and are presented below.

3.3.1. *Wall-normal-vorticity time scales*

The average event durations of ω_y above a unit r.m.s. were computed for the $R_\theta \simeq 2 \times 10^6$, relatively-smooth-wall $k_s^+ \approx 500$ six-wire data and $k_s^+ \approx 100$ four-wire data. Figure 9 shows the inner-normalized average event duration, $T^+(\omega_y)$, as a function of the distance from the wall. Inner-normalized event durations of $\partial u/\partial z$, computed using the data of Klewicki (1989*a*) at $R_\theta = 1010$ and 2870, are also shown for comparison. The $R_\theta = 2870$ $\partial u/\partial z$ event durations nominally merge with the present high-R_θ smooth-wall $k_s^+ \approx 100$ event durations. The $R_\theta = 1010$ $\partial u/\partial z$ event durations are, however, significantly lower than those at $R_\theta = 2870$. As shown, the inner-normalized event durations of ω_y for the present high-R_θ rough-wall data exhibit considerable scatter. The ω_y^+ event durations for the $k_s^+ \approx 100$ data are lower than those for the $k_s^+ \approx 500$ data. Overall, the data of figure 9 indicate both R_θ and wall-roughness influences.

Figure 10 shows the ω_y event durations divided by the locally defined Taylor time scales,

$$\lambda_t = \sqrt{\frac{2u'^2}{(\partial u/\partial t)'^2}}. \tag{3.2}$$

As per the suggestion of Klewicki & Falco (1996), the ratio of the vorticity event duration and λ_t produces a new function that is considerably less scattered. For comparison, event durations of $\partial u/\partial z$ divided by λ_t are shown for the data of Klewicki (1989*a*) at $R_\theta = 1010$ and 2870. As shown in figure 10, the event durations divided by λ_t appear to merge to a single curve that decreases with increasing y^+. More data at intermediate R_θ are required to clarify the relationship between the Taylor time scales and the ω_y event durations.

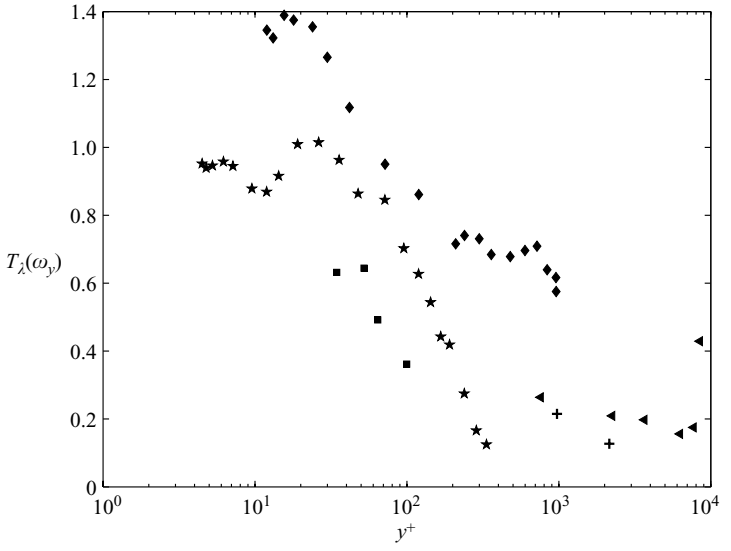

FIGURE 10. Taylor-microscale-normalized wall-normal-vorticity event durations as a function of y^+: ⋆, $T_\lambda(\partial u/\partial z)$ at $R_\theta = 1010$; ◆, $T_\lambda(\partial u/\partial z)$ at $R_\theta = 2870$. All the other symbols represent $T_\lambda(\omega_y)$ as defined in table 3.

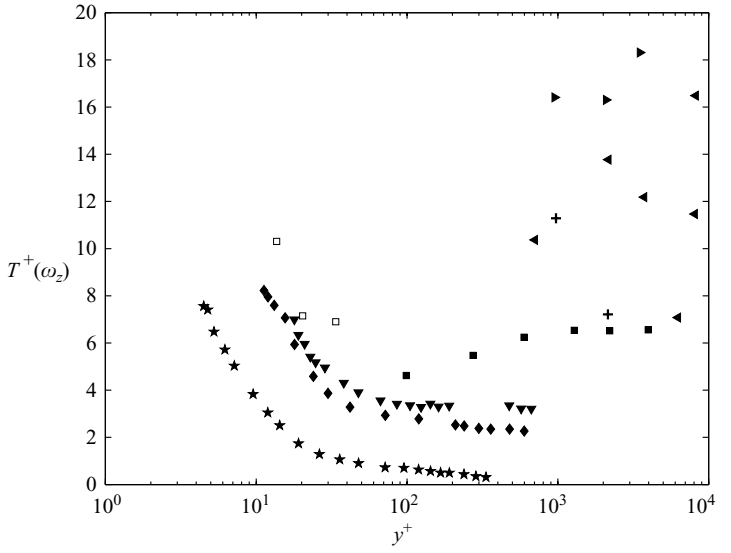

FIGURE 11. Inner-normalized spanwise-vorticity event duration as a function of y^+. The symbols are defined in table 3.

3.3.2. *Spanwise-vorticity time scales*

Figure 11 shows the inner-normalized average ω_z event durations as a function of distance from the wall. The ω_z event durations of Klewicki & Falco (1996) at $R_\theta = 1010$, 2870 and 4850 are also shown for comparison. $T^+(\omega_z)$ for the present relatively-smooth-wall data at $R_\theta \simeq 2 \times 10^6$ remains nearly constant with increasing y^+. A very similar trend is observed in $T^+(\omega_z)$ for the present $R_\theta \simeq 2 \times 10^6$ $k_s^+ \approx 500$, rough-wall results despite the scatter. The present $R_\theta \simeq 4 \times 10^6$ $k_s^+ \approx 300$ $T^+(\omega_z)$ data

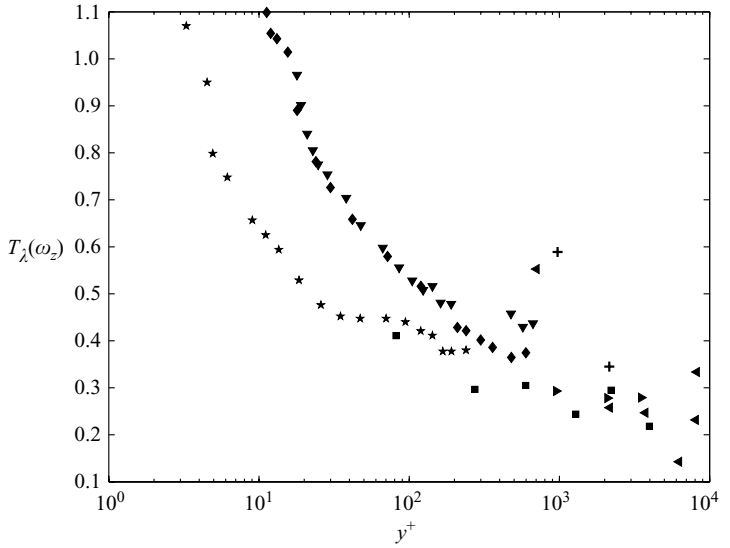

FIGURE 12. Taylor-microscale-normalized event durations of ω_z as a function of y^+. The symbols are defined in table 3.

are more significantly scattered. Nevertheless, they exhibit an identifiable increase in event durations when compared with the relatively-smooth-wall high-R_θ results. The present high-R_θ four-wire rough-wall $k_s^+ \approx 100$ data indicate lower values. From these observations it is concluded that the effects of both Reynolds number and surface roughness are at play. Overall, the smooth-wall data in this figure show that at any fixed R_θ and outside the near-wall region (say for $y^+ > 50$), the event durations exhibit very little variation with y^+. As is clearly shown, however, this nearly constant value increases with increasing R_θ and k_s^+.

Under outer normalization an R_θ trend opposite to that in figure 11 is observed (not shown). This indicates that the time scale of the event durations is intermediate to those for inner and outer scaling. As mentioned previously, Klewicki & Falco (1996) observed this behaviour for $1000 \lesssim R_\theta \lesssim 5000$ and explored the previously noted ratio of the event durations and the Taylor time scales λ_t. Event durations represented in this way are shown in figure 12. As indicated, the ratio of these functions for the present $R_\theta \simeq 2 \times 10^6$ $k_s^+ \approx 25 \sim 50$ data and the present $R_\theta \simeq 4 \times 10^6$ $k_s^+ \approx 300$ data appear to nominally merge into a single curve. The present $R_\theta \simeq 4 \times 10^6$ $k_s^+ \approx 100$ four-wire rough-wall ω_z data, however, provide slightly higher values. Similarly, the $R_\theta = 1010$ data of Klewicki (1989*a*) show lower values. The scatter in the high-R_θ rough-wall data, some of which may have been introduced by uncertainties in the U_τ estimates, has been considerably reduced. Overall, the results of figures 10 and 12 support the hypothesis that λ_t nominally serves as a characteristic time scale for the ω_y- and ω_z-bearing motions. A similar hypothesis was proposed by Falco (1977, 1983, 1991). That hypothesis was, however, based largely on the scale of vortical motions detected using flow visualization.

3.4. *Analysis of $v\omega_z$ signals*

3.4.1. *$v\omega_z$ statistics*

As can be seen in (1.4), $\overline{v\omega_z}$ is one of the two velocity–vorticity correlations contributing to $-\partial\overline{uv}/\partial y$. Figure 13 shows $\overline{v\omega_z}^+$ versus y^+ for the present high-R_θ

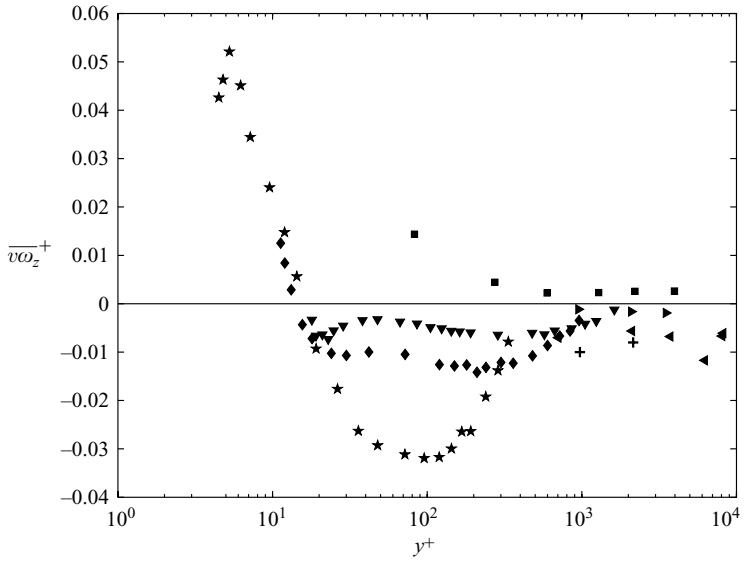

FIGURE 13. Distribution of inner-normalized $\overline{v\omega_z}$ as a function of y^+. The symbols are defined in table 3.

smooth- and rough-wall experiments. This figure also includes the previous low-R_θ results of Klewicki (1989*b*). At high-R_θ, all the data were acquired well within the inner region (the buffer and log-law regions). The $R_\theta \simeq 2\times10^6$ $k_s^+ \approx 25 \sim 50$ results exhibit positive correlations that appear to have consistency with the R_θ trend indicated by the low-R_θ data. Conversely, the high-R_θ rough-wall data show slightly negative correlations. The present high-R_θ four-wire data indicate more significant negative values. Thus, for smooth-wall turbulent boundary layers, the trend in figure 13 indicates that in the log layer $\overline{v\omega_z}^+$ increases with increasing R_θ (for $10^3 \lesssim R_\theta \lesssim 2\times10^6$). In relation to (1.4), the R_θ-dependence revealed in figure 13 indicates that as R_θ increases the contribution from $\overline{v\omega_z}$ to $-\overline{\partial uv}/\partial y$ (for the y^+ positions explored) changes from a relatively strong decelerating effect to a relatively weak accelerating effect in the axial mean-momentum balance. The addition of increasingly larger roughness appears to suppress this R_θ-dependence. This issue is analysed further through the spectral analysis in § 3.4.2.

The inner-normalized intensity $(v\omega_z)'^+$ of $v\omega_z$ is shown in figure 14. Previously unpublished low-R_θ $(v\omega_z)'^+$ data of Klewicki (1989*a*) are also shown for comparison. Most of the present high-R_θ smooth- and rough-wall data in $10^3 < y^+ < 10^4$ show $(v\omega_z)'^+$ values around 0.02. A few six-wire-probe and four-wire data points indicate significantly higher $(v\omega_z)'^+$ values. The present high-R_θ relatively- smooth-wall data in $100 < y^+ < 1000$ agree well with the low-R_θ data of Klewicki (1989*a*). There is also very little R_θ-dependence between the $R_\theta = 2870$ and $R_\theta = 4850$ data for $y^+ \gtrsim 30$. There are, however, significant differences exhibited by the data at $R_\theta = 1010$. As mentioned previously (in relation to other statistics), this may be a very-low-R_θ effect ($R_\theta \lesssim 1500$) (DeGraaff & Eaton 2000; Klewicki 1989*a*). As can be seen, the highest $(v\omega_z)^+$ fluctuations are observed in the near-wall region. In relation to the individual v and ω_z contributions, this is most likely due to the rapid increase in $\omega_z'^+$ near the wall (see figure 8), since v'^+ decreases as $y \to 0$.

Profiles for the v–ω_z correlation coefficient $\rho_{v\omega_z}$ are shown in figure 15. For comparison, the $1000 \lesssim R_\theta \lesssim 5000$ results of Klewicki (1989*a*) (previously unpublished) as

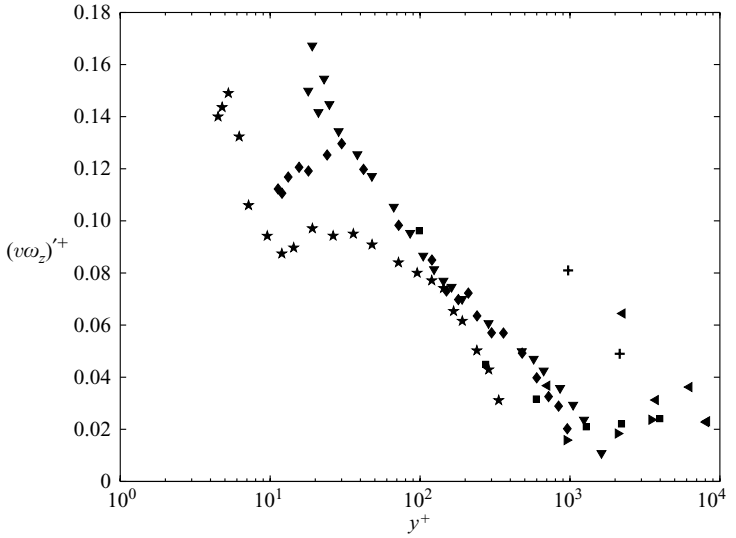

FIGURE 14. Distribution of inner-normalized $v\omega_z$ intensity as a function of y^+. The symbols are defined in table 3.

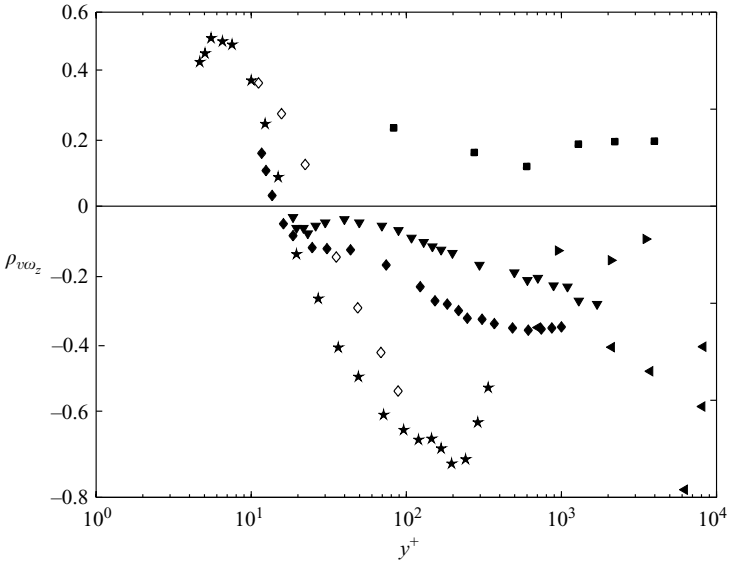

FIGURE 15. The correlation coefficient $\rho_{v\omega_z}$ as a function of y^+. The symbols are defined in table 3.

well as the $R_\theta = 1450$ results of Rajagopalan & Antonia (1993) are also shown. The R_θ-dependences exhibited in figure 13 are further exemplified and more clearly illustrated here. The present $R_\theta \simeq 2 \times 10^6$ relatively-smooth-wall $\rho_{v\omega_z}$ results are positive, reaching a significant magnitude near 0.2. Conversely, almost all the present $R_\theta \simeq 2 \times 10^6$ $k_s^+ \approx 500$ results are negative, with values near -0.4. The present $k_s^+ \approx 100$ four-wire data show negative correlation coefficients around -0.2. Notable features in figure 15 are (*a*) an apparent merging of the $\rho_{v\omega_z}$ profiles for different R_θ for $y^+ \lesssim 15$, (*b*) the relatively large values of $|\rho_{v\omega_z}|$ in the log layer (at any R_θ, but especially at low-R_θ) and

(*c*) the aforementioned change in sign of $\rho_{v\omega_z}$ at high R_θ. In relation to scale-separation effects, the third of these is particularly significant, since it depends upon the degree of interaction between the v and ω_z fluctuations. This issue is further addressed in the spectral analyses below. The high-R_θ $k_s^+ \approx 500$ data exhibit significantly negative values. On the basis of the observed sensitivity of v'^+ to roughness relative to that of $\omega_z'^+$ (see figures 4 and 8 respectively), it is anticipated that this observed sensitivity of $v\omega_z$ is derived more from the modification of the velocity field than the vorticity field.

3.4.2. *Spectral structure of* $v\omega_z$

Spectral analyses of v and ω_z are presented in this section. The inner-normalized wall-normal-velocity power spectra $\Phi^+(v)$ and the inner-normalized spanwise-vorticity power spectra $\Phi^+(\omega_z)$ were computed using the method explained in § 2.4.4. These power spectra were multiplied by the inner-normalized streamwise wavenumber k^+ to obtain the premultiplied power spectra of v and ω_z, $\Psi^+(v)$ and $\Psi^+(\omega_z)$, respectively. The inner-normalized wavenumber was computed using

$$k^+ = 2\pi \frac{\overline{f}^+}{\overline{U}^+}, \tag{3.3}$$

where $\overline{U}^+ (= \overline{U}/U_\tau)$ is the inner-normalized mean advection velocity and $f^+ (= f\nu/U_\tau^2)$ is the inner-normalized frequency. The methods described in § 2.4.4 were also used to compute the cospectrum of v and ω_z, $\Lambda^+(v\omega_z)$, and the premultiplied cospectrum, $k^+\Lambda^+(v\omega_z)$. Figure 16(*a–d*) shows $\Psi^+(v)$, $\Psi^+(\omega_z)$ and $k^+\Lambda^+(v\omega_z)$ at a wall-normal location near $y_p/2$ for $R_\theta = 2870$, $R_\theta = 4850$, $R_\theta \simeq 2 \times 10^6$, $k_s^+ \approx 25 \sim 50$, and $R_\theta \simeq 4 \times 10^6$, $k_s^+ \approx 300$. As previously mentioned, y_p is the estimated wall-normal position of the peak in $-\overline{uv}^+$. The abscissa in figures 16(*a–d*) is the inner-normalized wavenumber k^+ and the ordinate is the premultiplied spectral density.

As shown in figure 16(*a*), $\Psi^+(v)$, and $\Psi^+(\omega_z)$ for $R_\theta = 2870$ lie nearly on top of each other at $y_p/2$. The peaks in these spectra occur at slightly lower wavenumbers than the inner-normalized Taylor wavenumber, $2\pi/\lambda^+ = k_\lambda^+ \approx 0.07$. Figure 16(*a*) indicates that $k^+\Lambda^+(v\omega_z)$ inversely tracks $\Psi^+(\omega_z)$ for wavenumbers $\gtrsim k_\lambda^+$. Starting at scales slightly larger than the peak in $\Psi^+(\omega_z)$, v and ω_z exhibit a strong negative correlation that is large compared with the positive correlations at higher wavenumber. The results for $R_\theta = 4850$ are similar to those at $R_\theta = 2870$. For $R_\theta = 4850$, $\Psi^+(v)$ and $\Psi^+(\omega_z)$ closely track each other at $y_p/2$. The behaviour of $k^+\Lambda^+(v\omega_z)$ is also similar. The small-scale motions of the $v\,\omega_z$ product (having wavenumbers near the peak in $\Psi^+(\omega_z)$; see curve (r)), however, exhibit a larger positive peak than that at $R_\theta = 2870$.

The results near $y_p/2$ for $R_\theta \simeq 2 \times 10^6$, $k_s^+ \approx 25 \sim 50$ and for $R_\theta \simeq 4 \times 10^6$, $k_s^+ \approx 300$ are presented in figures 16(*c*) and 16(*d*), respectively. The behaviour of $\Psi^+(\omega_z)$ changes somewhat at high-R_θ. Most notably, the peak in $\Psi^+(\omega_z)$ at high-R_θ occurs at a wavenumber slightly higher than k_λ. The apparent effects of wall roughness on $k^+\Lambda^+(v\omega_z)$ for $R_\theta \simeq 2 \times 10^6$, $k_s^+ \approx 25 \sim 50$ are minimal when compared with those at $R_\theta \simeq 4 \times 10^6$, $k_s^+ \approx 300$. As shown in figure 16(*c*), $k^+\Lambda^+(v\omega_z)$ at $y_p/2$ nominally tracks $\Psi^+(\omega_z)$ at all wavenumbers. The peak of $k^+\Lambda^+(v\omega_z)$ is very close to the peak of $\Psi^+(\omega_z)$, which occurs near k_λ^+. At relatively low wavenumbers $k^+\Lambda^+(v\omega_z)$ shows some evidence of tracking $\Psi^+(v)$ near its peak. The magnitudes of $k^+\Lambda^+(v\omega_z)$ are, however, relatively small at low k^+. Thus, at $y_p/2$, the high-R_θ relatively-smooth-wall flow has its peak contribution to $\overline{v\omega_z}$ near k_λ^+. This finding is very similar to that previously reported by Priyadarshana & Klewicki (2004*a*).

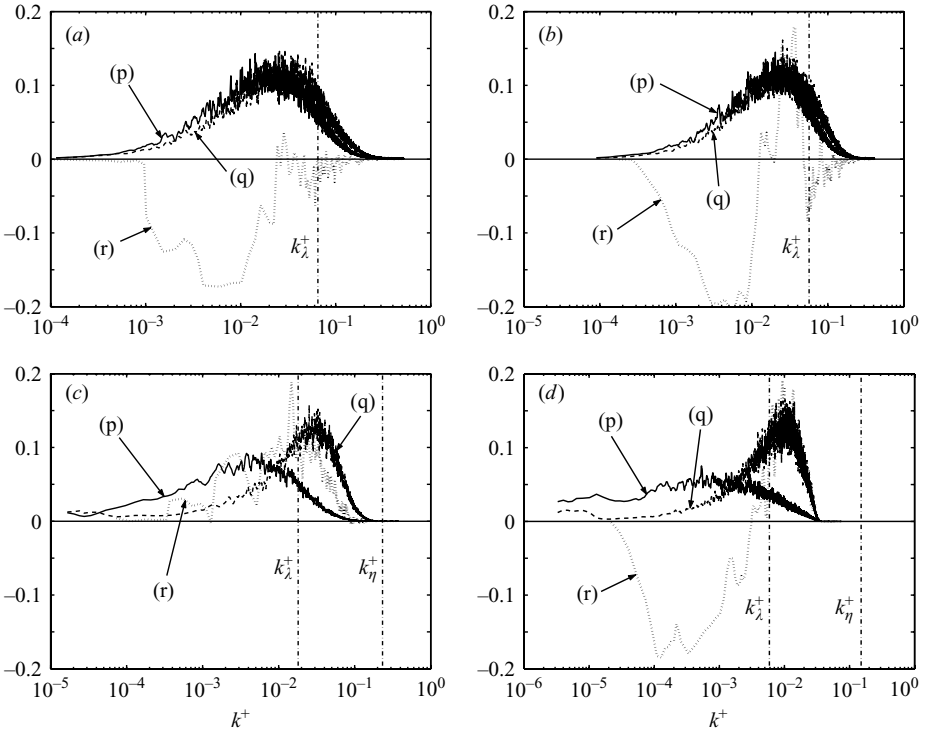

FIGURE 16. Premultiplied power spectra $\Psi^+(v)$ and $\Psi^+(\omega_z)$ of v^+ and ω_z^+ and premultiplied cospectra $k^+\Lambda^+(v\omega_z)$ of v^+ and ω_z^+, near $y_p/2$: (p), $\Psi^+(v)$; (q), $\Psi^+(\omega_z)$; (r), $k^+\Lambda^+(v\omega_z)$. (*a*) $R_\theta = 2870$, smooth-wall ($y^+ = 30$); (*b*) $R_\theta = 4850$, smooth-wall ($y^+ = 38$); (*c*) $R_\theta \simeq 2 \times 10^6$, $k_s^+ \approx 25 \sim 50$ ($y^+ = 660$); (*d*) $R_\theta \simeq 4 \times 10^6$, $k_s^+ \approx 300$ ($y^+ = 1030$).

As shown in figure 16(*d*), the above behaviour changes significantly at $y_p/2$ with the introduction of wall roughness ($k_s^+ \approx 300$). Note that at this Reynolds number, y_p ($y^+ = 1030$) is estimated to be near the edge of the roughness sublayer. The $\Psi^+(\omega_z)$ and $\Psi^+(v)$ results in figure 16(*d*) are very similar to those in figure 16(*c*). Similarly, the high-wavenumber portion of the rough-wall $k^+\Lambda^+(v\omega_z)$ is similar to that for the relatively-smooth-wall data at $R_\theta \simeq 2 \times 10^6$, in that it nominally tracks $\Psi^+(\omega_z)$. At low wavenumbers, however, $k^+\Lambda^+(v\omega_z)$ exhibits a large negative peak at a wavenumber very close to the peak of $\Psi^+(v)$. Thus, at $y_p/2$ the larger-scale motions of v and ω_z tend to correlate negatively with increasing wall roughness. The area under the negative portion of $k^+\Lambda^+(v\omega_z)$ is significantly greater than the positive portion of $k^+\Lambda^+(v\omega_z)$ and, thus, $\overline{v\omega_z}^+$ and $\rho_{v\omega_z}$ are negative (see figures 13 and 15).

The premultiplied v and ω_z spectra and cospectra near $2y_p$ are shown in figure 17. As can be seen, the premultiplied spectra at $2y_p$ differ considerably from those at $y_p/2$. This said, it should be noted that $y_p/2$ is within the buffer layer at $R_\theta = 2870$ and 4850. (Note that, at higher R_θ, $y_p/2$ is in the log-law region.) The location of $2y_p$ is in the log layer for all R_θ. At this location, the peaks in $\Psi^+(v)$ and $\Psi^+(\omega_z)$ achieve about 0.2 decades of scale separation at $R_\theta = 4850$ and slightly less than that at $R_\theta = 2870$. It is also interesting to note that the peak in $\Psi^+(\omega_z)$ is located near the Taylor wavenumber at $R_\theta = 4850$ and at a slightly lower k^+ value at $R_\theta = 2870$. At both Reynolds numbers, the position of the negative peak in $k^+\Lambda^+(v\omega_z)$ closely tracks

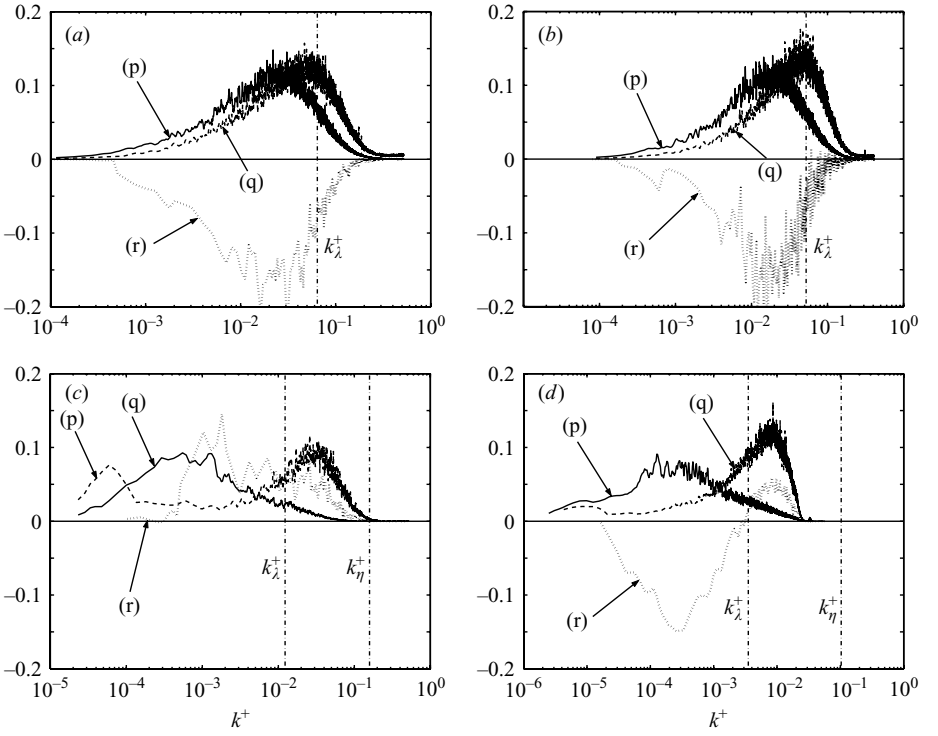

FIGURE 17. Premultiplied power spectra $\Psi^+(v)$ and $\Psi^+(\omega_z)$ of v and ω_z and premultiplied cospectra $k^+\Lambda^+(v\omega_z)$ of v^+ and ω_z^+, near $2y_p$: (p), $\Psi^+(v)$; (q), $\Psi^+(\omega_z)$; (r), $k^+\Lambda^+(v\omega_z)$. (*a*) $R_\theta = 2870$, smooth-wall ($y^+ = 120$); (*b*) $R_\theta = 4850$, smooth-wall ($y^+ = 143$); (*c*) $R_\theta \simeq 2 \times 10^6$, $k_s^+ \approx 25 \sim 50$ ($y^+ = 4010$); (*d*) $R_\theta \simeq 4 \times 10^6$, $k_s^+ \approx 300$ ($y^+ = 3800$).

the position of the positive peak of $\Psi^+(v)$. This occurs at a wavenumber $0.4 \sim 0.5$ decades lower than the Taylor wavenumber.

Figure 17(*c*) reveals that the behaviour of the high-R_θ relatively-smooth-wall $k^+\Lambda^+(v\omega_z)$ is significantly different at $2y_p$. There is a relatively-low-wavenumber peak in $k^+\Lambda^+(v\omega_z)$ that appears to nominally track the peak of $\Psi^+(v)$. Unlike the low-R_θ results, however, this peak is positive. Consistently with the results at $y_p/2$, there is also a small second peak of $k^+\Lambda^+(v\omega_z)$ at high wavenumber. The amplitude of this second peak is significantly attenuated relative to that at $y_p/2$. Thus, in the high-R_θ relatively-smooth-wall flow, the peak contribution to $\overline{v\omega_z}^+$ shifts from relatively small scales to relatively large scales for a shift in the wall-normal location from $y_p/2$ to $2y_p$. It is, however, important to note that the peak in $\Psi^+(v)$ is still at a wavenumber that is at least an order of magnitude higher than the wavenumber of the peak in $\Psi^+(u)$ (Priyadarshana & Klewicki 2004*b*). The rough-wall $k^+\Lambda^+(v\omega_z)$ exhibits similarities to that at $y_p/2$. As shown in figure 17(*d*), the low-wavenumber motions of v and ω_z are negatively correlated, giving a negative peak similar to that observed at $y_p/2$. The amplitude of the high-wavenumber peak in $k^+\Lambda^+(v\omega_z)$ is reduced similarly to that under the smoother wall condition. Overall, the high-wavenumber peak in the high-R_θ rough-wall $k^+\Lambda^+(v\omega_z)$ tracks $\Psi^+(\omega_z)$.

The wavenumbers at which the smooth-wall premultiplied power spectra attain their peak values were obtained using a third-order polynomial curve-fit in the vicinity of the peak. Here, $k^+_{max(\Psi^+(v))}$ and $k^+_{max(\Psi^+(\omega_z))}$ are the inner-normalized wavenumbers at

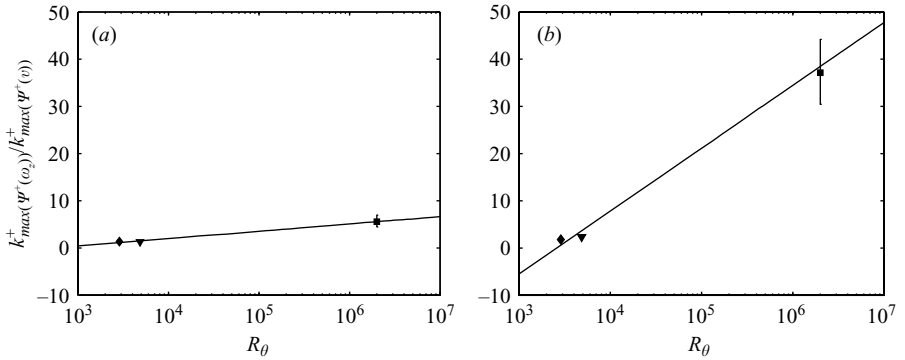

FIGURE 18. Variation in $k^+_{max(\Psi^+(\omega_z))}/k^+_{max(\Psi^+(v))}$ as a function of R_θ. The symbols are defined in table 3. (*a*) Variation near $y_p/2$. The curve-fit shown is $k^+_{max(\Psi^+(\omega_z))}/k^+_{max(\Psi^+(v))} = 1.55\log R_\theta - 4.2$. (*b*) Variation near $2y_p$. The curve-fit shown is $k^+_{max(\Psi^+(\omega_z))}/k^+_{max(\Psi^+(v))} = 13.3\log R_\theta - 45.4$.

which $\Psi^+(v)$ and $\Psi^+(\omega_z)$ peak, respectively. To quantify scale-separation effects on the momentum transport, the ratio of these two wavenumbers, $k^+_{max(\Psi^+(\omega_z))}/k^+_{max(\Psi^+(v))}$, was plotted against R_θ as shown in figure 18. Figure 18(*a*) describes the variation in $k^+_{max(\Psi^+(\omega_z))}/k^+_{max(\Psi^+(v))}$ as a function of R_θ at $y_p/2$ and figure 18(*b*) describes the same at $2y_p$. As shown, both variations for low-R_θ smooth-wall and high-R_θ relatively-smooth-wall data are nominally fitted by a logarithmic relationship. Obviously, more intermediate R_θ data are required to clarify fully this R_θ-dependence.

3.5. *Analysis of $w\omega_y$ signals*

This section describes the statistics and spectra of the w and ω_y fluctuations. The data used in these studies were acquired using the six-element v-array probe and four-wire probes. The data from the six-element v-array probe were acquired under rough-wall conditions at $R_\theta \simeq 2\times10^6$ with an inner-normalized wall roughness of $k_s^+ \approx 500$ and under relatively-smooth-wall conditions at $R_\theta \simeq 2\times10^6$ with $k_s^+ \simeq 25\sim50$. The data from the four-wire probes were acquired at $R_\theta \simeq 4\times10^6$ with an inner-normalized wall roughness of $k_s^+ \approx 100$.

3.5.1. *Analysis of $w\omega_y$ statistics*

The present $\overline{w\omega_y}^+$ data are shown in figure 19. The near-wall $R_\theta \simeq 2\times10^6$ data ($k_s^+ \approx 25\sim50$) show negative $\overline{w\omega_y}^+$ values around $-0.07\sim-0.06$ in the region $40 < y^+ < 70$. These data continue to increase significantly for $y^+ > 100$ and meld into the $R_\theta \simeq 2\times10^6$ $k_s^+ \approx 500$ data that cross zero near $y^+ = 700$. A very similar trend is observed in the present four-wire $k_s^+ \approx 100$ data. The previous $\overline{w\omega_y}^+$ estimates of Klewicki (1989*b*) and the low-R_θ DNS data of Crawford & Karniadakis (1997) are also shown for comparison. The $\overline{w\omega_y}^+$ profiles of Klewicki (1989*b*) were derived using the available $\overline{v\omega_z}^+$ and $-\partial\overline{(uv)}^+/\partial y^+$ data. The data of Crawford & Karniadakis (1997) at $Re_H = 5000$, where H is the channel height and Re_H is the Reynolds number based on the channel height, show a negative peak at $y^+ \simeq 10$ and follow the $R_\theta = 2870$ and 4850 profiles of Klewicki (1989*b*). Similarly, the present relatively-smooth-wall and rough-wall high-R_θ data follow the indicated trend. Again, the near-wall data of Klewicki (1989*b*) at $R_\theta = 1010$ show some scattered behaviours. These could be very-low-R_θ effects or the uncertainties associated with obtaining $\overline{w\omega_y}^+$ estimates.

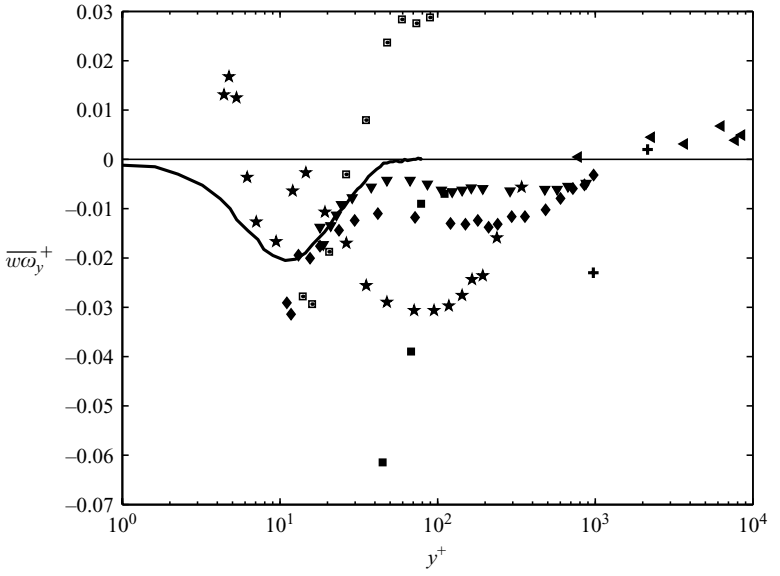

FIGURE 19. Distribution of inner-normalized $\overline{w\omega_y}$ as a function of y^+. The symbols are defined in table 3.

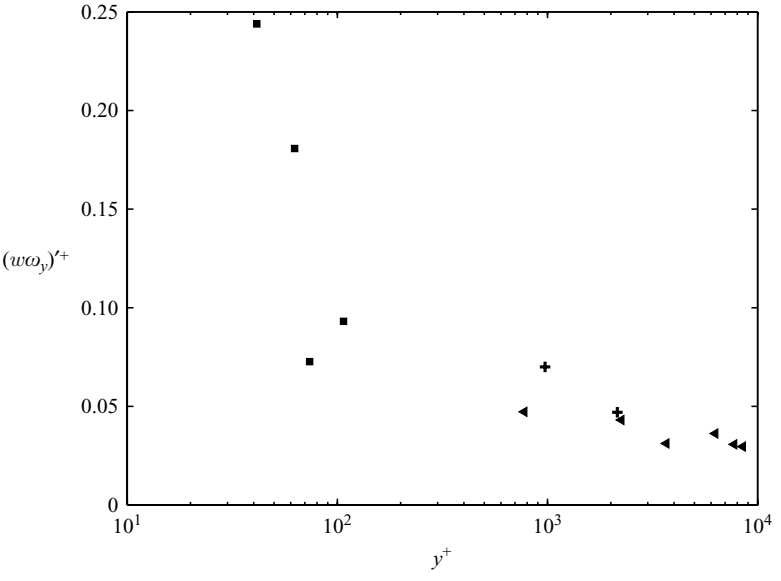

FIGURE 20. Distribution of inner-normalized $w\omega_y$ intensity as a function of y^+. The symbols are defined in table 3.

The inner-normalized intensity $(w\omega_y)'^+$ of $w\omega_y$ is shown in figure 20. As indicated, the largest values of $(w\omega_y)'^+$ are observed in the relatively-smooth-wall data closer to the wall. The intensity decreases with increasing y^+. The rough-wall data follow the same trend away from the wall. Furthermore, the present $k_s^+ \approx 500$ rough-wall data agree well with the present $k_s^+ \approx 100$ four-wire data. Overall, the behaviour of $(w\omega_y)'^+$ is similar to that displayed by $(v\omega_z)'^+$, discussed in § 3.4.1.

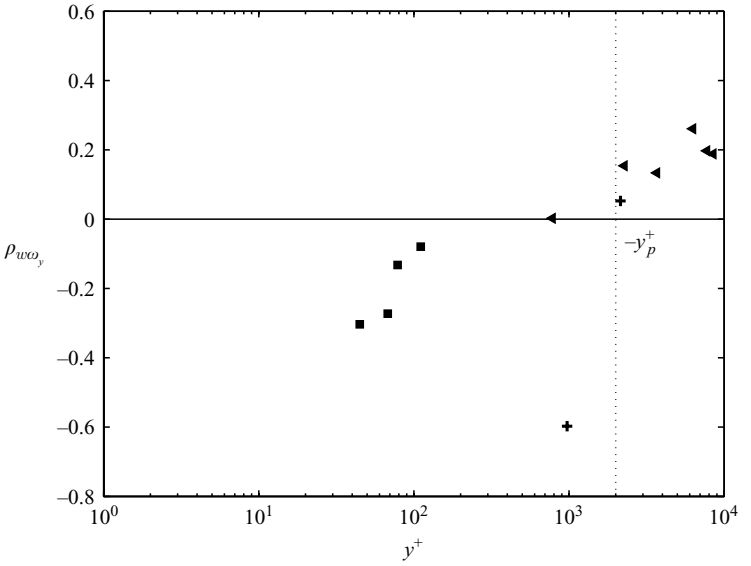

FIGURE 21. The correlation coefficient $\rho_{w\omega_y}$ as a function of y^+. The symbols are defined in table 3.

The profiles of the w–ω_y correlation coefficient $\rho_{w\omega_y}$ are shown in figure 21. The negative and positive correlations between w and ω_y exhibited in figure 19 are further exemplified and more clearly illustrated in this figure. Near the wall, these results show strong negative correlations, attaining values near -0.3. Conversely, all the present $R_\theta \simeq 2 \times 10^6$ $k_s^+ \approx 500$ $\rho_{w\omega_y}$ results away from the wall are positive, with values near 0.2. The zero crossing in the correlation coefficient is at around $y^+ = 1000$ and thus occurs relatively close to y_p^+. A zero crossing in $\overline{w\omega_y}^+$ at y_p^+ is consistent with (1.4), in that $\partial\overline{uv}/\partial y$ changes sign as well. This issue is further addressed in the spectral analyses below in § 3.5.2.

3.5.2. *Spectral analysis of* $w\omega_y$

Spectral information associated with w and ω_y is presented in this section. As before, the inner-normalized spanwise-velocity power spectra $\Phi^+(w)$ and the inner-normalized wall-normal-vorticity power spectra $\Phi^+(\omega_y)$ were computed using the method explained in § 2.4.4. These power spectra were multiplied by the inner-normalized wavenumber k^+ to obtain the premultiplied power spectra $\Psi^+(w)$ and $\Psi^+(\omega_y)$. The same methods were used to compute the inner-normalized cospectrum $\Lambda^+(w\omega_y)$ and the premultiplied inner-normalized cospectrum $k^+\Lambda^+(w\omega_y)$.

Figure 22(a,b) shows $\Psi^+(w)$, $\Psi^+(\omega_y)$ and $k^+\Lambda^+(w\omega_y)$ at wall-normal locations near $y_p/2$ and $2y_p$ for $R_\theta \simeq 2 \times 10^6$, $k_s^+ \approx 500$. As shown in figure 22(a), $\Psi^+(\omega_y)$ has a peak at a slightly higher wavenumber than k_λ^+ and $\Psi^+(w)$ has a peak around $k^+ \simeq 10^{-3}$, which is very close to the peaks of $\Psi^+(v)$ shown in figures 16(c) and 16(d). The peak wavenumbers of $\Psi^+(w)$ and $\Psi^+(\omega_y)$ are separated by at least two orders of magnitude. Figure 22(a) indicates that $k^+\Lambda^+(w\omega_y)$ inversely tracks $\Psi^+(\omega_y)$. This is similar to the behaviour of $k^+\Lambda^+(v\omega_z)$ at $R_\theta \simeq 2 \times 10^6$. The tracking is, however, positively correlated in the $v\omega_z$ case.

Near $2y_p$ the peak in $\Psi^+(w)$ moves to lower wavenumbers, while the peak in $\Psi^+(\omega_y)$ remains near the Taylor wavenumber. The premultiplied cospectrum $k^+\Lambda^+(w\omega_y)$ has

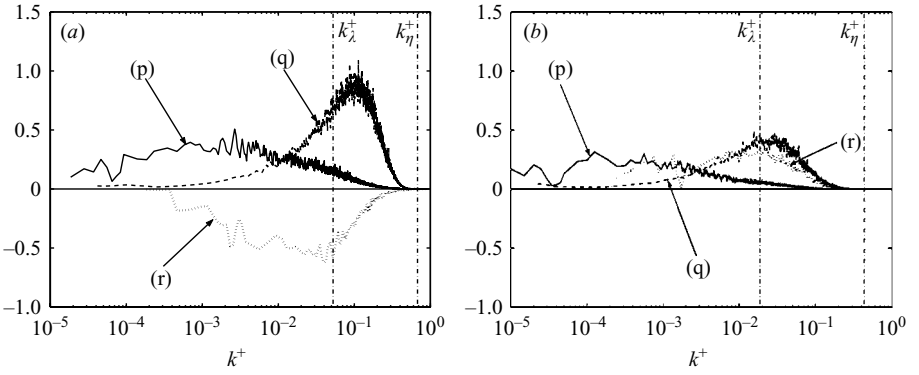

FIGURE 22. Premultiplied power spectra $\Psi^+(w)$ and $\Psi^+(\omega_y)$ of w and ω_y and premultiplied cospectra $k^+\Lambda^+(w\omega_y)$ of w^+ and ω_y^+ at wall-normal locations (*a*) $y_p/2$ and (*b*) $2y_p$: (p), $\Psi^+(w)$; (q), $\Psi^+(\omega_y)$; (r), $k^+\Lambda^+(w\omega_y)$. (*a*) $R_e \simeq 2\times10^6$, $k_s^+ \approx 500$, $y_p/2\,(y^+ = 924)$. (*b*) $R_e \simeq 2\times10^6$, $k_s^+ \approx 500$, $2y_p\,(y^+ = 4200)$.

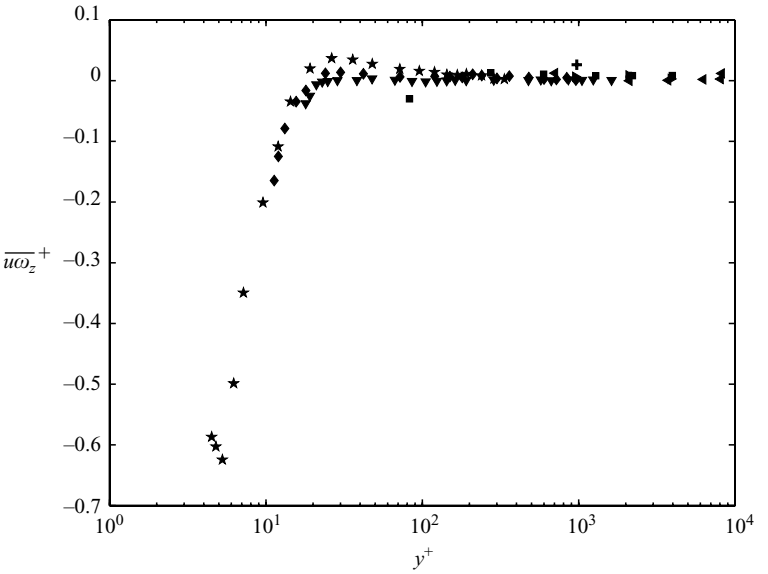

FIGURE 23. Distribution of inner-normalized $\overline{u\omega_z}$ as a function of y^+. The symbols are defined in table 3.

two positive peaks at $2y_p$. One peak tracks $\Psi^+(\omega_y)$ and the other peak tracks $\Psi^+(w)$. This behaviour is the underlying reason why $\overline{w\omega_y}^+$ is positive for $y > y_p$.

3.6. *Analysis of $u\omega_z$ signals*

Statistics and spectral analyses were conducted in relation to the u and ω_z signals for the same R_θ and wall-roughness conditions as in the $v\omega_z$ and $w\omega_y$ analyses.

3.6.1. *Analysis of $u\omega_z$ statistics*

The distributions of $\overline{u\omega_z}^+$ with y^+ are shown in figure 23 for the present high-R_θ data. These results are compared with the low-R_θ results of Klewicki (1989*b*). The present six-wire high-R_θ data meld smoothly with the low-R_θ data regardless of the surface roughness. As noted by Klewicki (1989*b*), the $R_\theta = 1010$ results show a small

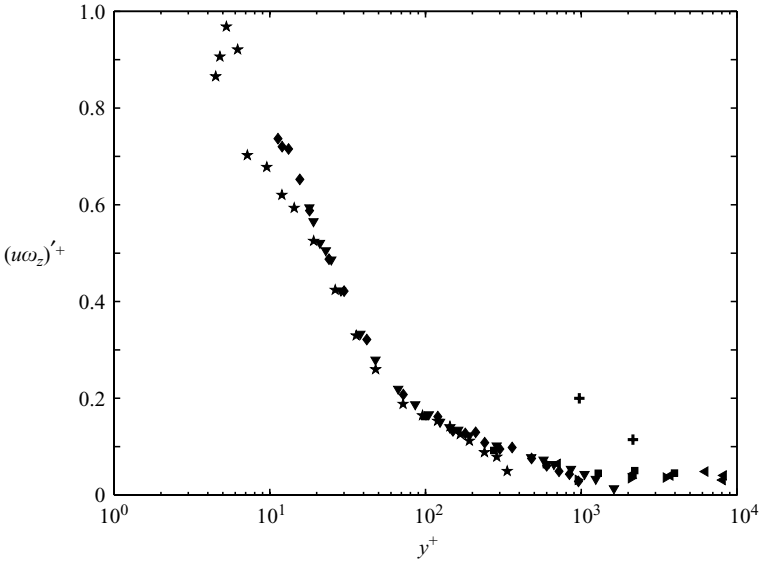

FIGURE 24. Distribution of inner-normalized $u\omega_z$ intensity as a function of y^+. The symbols are defined in table 3.

deviation from the other curves in the buffer layer. Other than this, there are no apparent effects of surface roughness and/or R_θ in $\overline{u\omega_z}^+$ for the k_s^+, y^+ and R_θ conditions explored.

The present high-R_θ inner-normalized intensity $(u\omega_z)'^+$ of $u\omega_z$ is shown in figure 24. Previously unpublished results of Klewicki (1989*a*) are also given, for comparison. Similarly to the $(v\omega_z)'^+$ and $(w\omega_y)'^+$ results, the largest values of $(u\omega_z)'^+$ are observed in the near-wall region. As shown, the present six-wire high-R_θ data in the log-law region tend to meld into the $R_\theta = 2870$ and 4850 data near $y^+ = 100$. The present four-wire data show higher $(u\omega_z)'^+$ values. As with $\overline{u\omega_z}^+$, it may be concluded that the inner-normalized $(u\omega_z)'$ is not very sensitive to R_θ or the surface roughness.

The u–ω_z correlation coefficient, $\rho_{u\omega_z}$ is presented in figure 25. The results of Rajagopalan & Antonia (1993) at $R_\theta = 1450$ nominally agree with those of Klewicki (1989*a*) at $R_\theta = 1010$. Both these profiles show strong negative values in the buffer layer. Farther from the wall these data exhibit a positive peak in the range $0.1 \sim 0.15$. With increasing R_θ, this peak value decreases. The present high-R_θ $\rho_{u\omega_z}$ data are scattered. The data centre around 0.1 in the log layer. In this regard, it is worth noting that while the four-wire-probe results (the + symbols) show distinctly higher-magnitude values of $(u\omega_z)'^+$ than the six-wire results, the $\overline{u\omega_z}^+$ and $\rho_{u\omega_z}$ results from the two sensors are in very good agreement. The origin of the apparent proportional increase in $(u\omega_z)'^+$ from the four-wire probe is, at present, unknown. Overall, there is very little apparent effect of surface roughness on $\rho_{u\omega_z}$.

3.6.2. *Spectral analysis of* $u\omega_z$

Figure 26(*a–d*) shows the inner-normalized premultiplied power spectra $\Psi^+(u)$ and $\Psi^+(\omega_z)$ and the inner-normalized premultiplied cospectra $k^+\Lambda^+(u\omega_z)$ near $y_p/2$. As shown in figure 26(*a*), $\Psi^+(u)$ for $R_\theta = 2870$ and $y_p/2$ peaks at a relatively low wavenumber whereas, as shown previously, $\Psi^+(\omega_z)$ peaks near the Taylor wavenumber. Even at this low-R_θ, the inner-normalized wavenumbers of these two peaks are separated by about one decade. The cospectra at $R_\theta = 2870$ has two peaks:

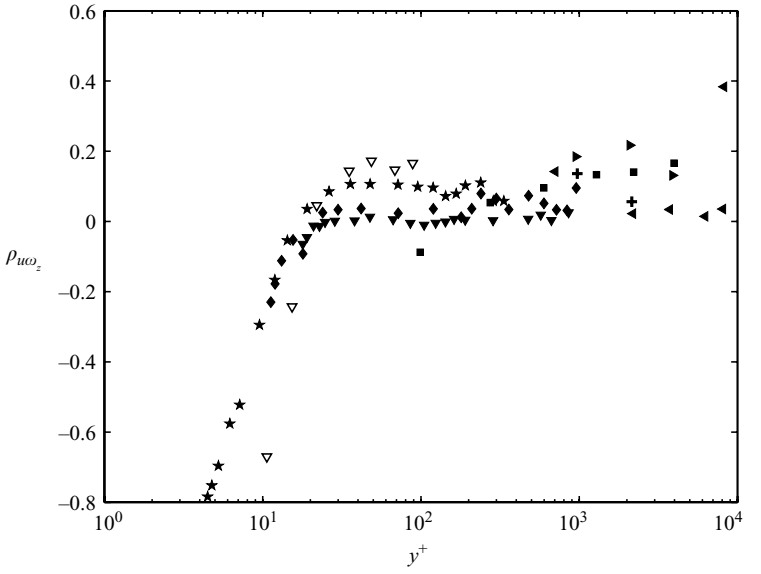

FIGURE 25. Profiles of $\rho_{u\omega_z}$ as a function of y^+. The symbols are defined in table 3.

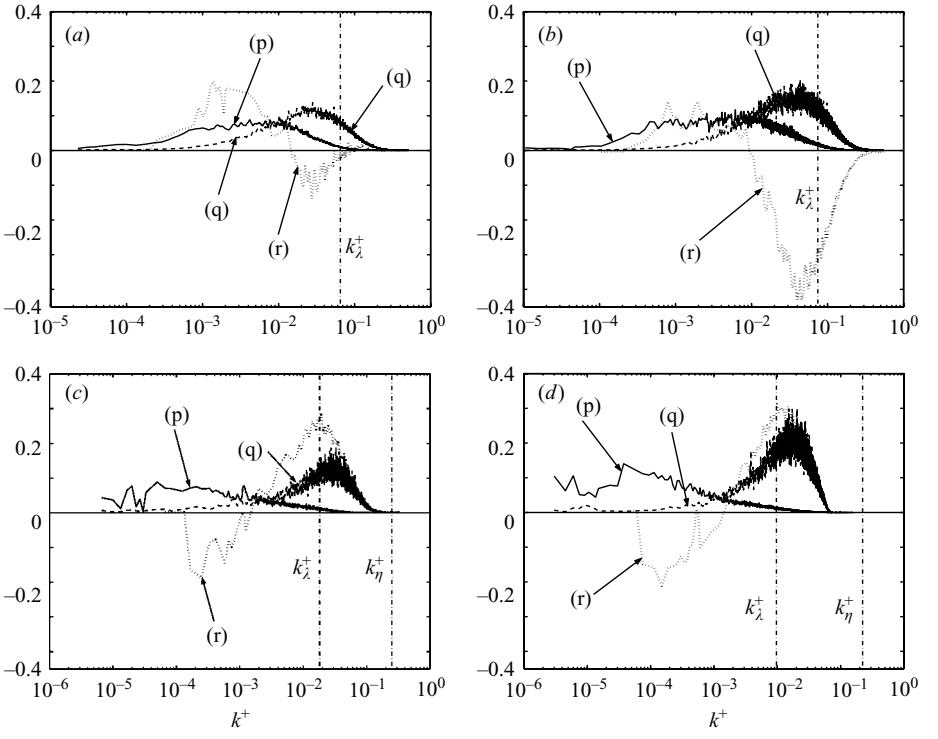

FIGURE 26. Premultiplied power spectra $\Psi^+(u)$ and $\Psi^+(\omega_z)$ of u^+ and ω_z^+ and premultiplied cospectra $k^+\Lambda^+(u\omega_z)$ of u^+ and ω_z^+ near $y_p/2$: (p), $\Psi^+(u)$; (q), $\Psi^+(\omega_z)$; (r), $k^+\Lambda^+(u\omega_z)$. (*a*) $R_\theta = 2870$, smooth-wall ($y^+ = 30$); (*b*) $R_\theta = 4850$, smooth-wall ($y^+ = 38$); (*c*) $R_\theta \simeq 2 \times 10^6$, $k_s^+ \approx 25 \sim 50 (y^+ = 660)$; (*d*) $R_\theta \simeq 4 \times 10^6$, $k_s^+ \approx 300\,50\,(y^+ = 1030)$.

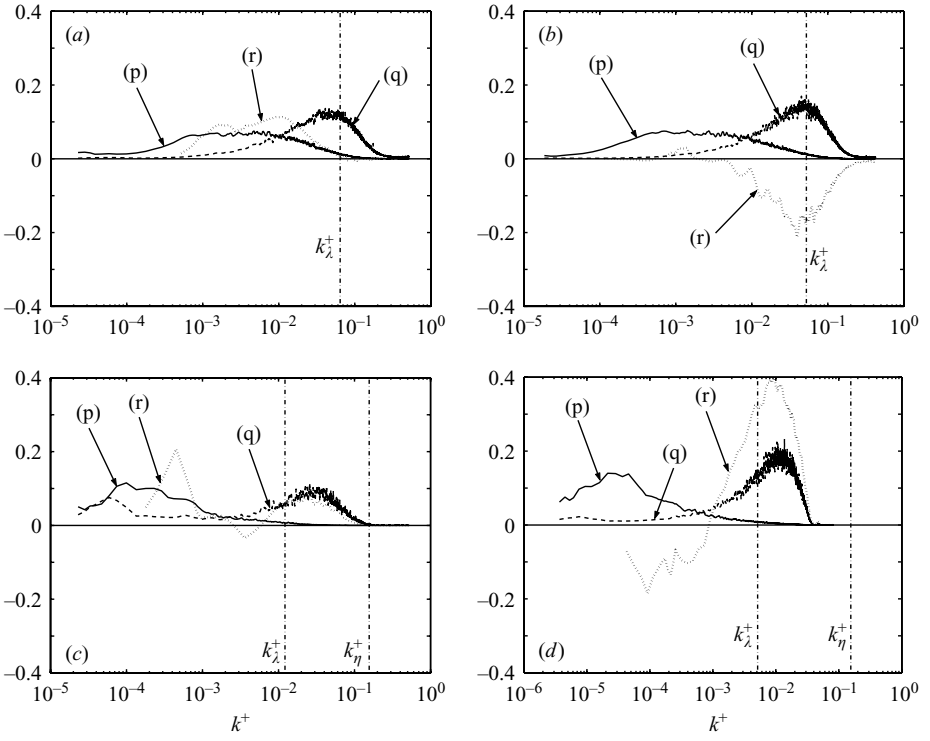

FIGURE 27. Premultiplied power spectra $\Psi^+(u)$ and $\Psi^+(\omega_z)$ of u and ω_z, and premultiplied cospectra $k^+\Lambda^+(u\omega_z)$ of u^+ and ω_z^+, at wall-normal location of $2y_p$: (p), $\Psi^+(u)$; (q) $\Psi^+(\omega_z)$; (r), $k^+\Lambda^+(u\omega_z)$. (*a*) $R_\theta = 2870$ ($y^+ = 120$); (*b*) $R_\theta = 4850$ ($y^+ = 143$); (*c*) $R_\theta \cong 2 \times 10^6$, $k_s^+ \approx 25 \sim 50$ ($y^+ = 4010$); (*d*) $R_\theta \cong 4 \times 10^6$, $k_s^+ \approx 300$ ($y^+ = 3800$).

the positive peak nominally aligns with the peak in $\Psi^+(u)$, and the negative peak nominally aligns with the peak in $\Psi^+(\omega_z)$. A largely similar behaviour is observed at $R_\theta = 4850$. In this case, the negative peak in $k^+\Lambda^+(u\omega_z)$ is of significantly higher amplitude. Similarly to $k^+\Lambda^+(u\omega_z)$ at $R_\theta = 2870$, the low-wavenumber motions of u and ω_z are positively correlated.

For the high-R_θ cases, the peak in $\Psi^+(u)$ shifts to significantly lower wavenumbers. In direct contrast with the negative correlation at low-R_θ, all the high-wavenumber motions of u and ω_z in figure 26(*c*) are highly positively correlated. Recall that $\overline{u\omega_z}^+ \approx 0$ for all R_θ values at this wall-normal location; see figure 23. The results in figure 26(*d*) are very similar to those in figure 26(*c*) specifically relating to the positive correlations at high wavenumbers and negative correlations at low wavenumbers.

Figure 27(*a–d*) shows $\Psi^+(u)$, $\Psi^+(\omega_z)$ and $k^+\Lambda^+(u\omega_z)$ near $2y_p$. In concert with the previously noted shift in $\Psi^+(\omega_z)$ towards higher wavenumbers, the peaks in $\Psi^+(u)$ move to even lower wavenumbers owing to the prevalence of relatively lower-wavenumber u-motions with increasing y. The $R_\theta = 2870$ results reveal a broad peak in $k^+\Lambda^+(u\omega_z)$, nominally positioned between the two peaks of $\Psi^+(u)$ and $\Psi^+(\omega_z)$. At $R_\theta = 4850$, $k^+\Lambda^+(u\omega_z)$ exhibits a single dominant negative peak that nominally mirrors the shape of $\Psi^+(\omega_z)$.

Figure 27(*c–d*) shows $\Psi^+(u)$, $\Psi^+(\omega_z)$ and $k^+\Lambda^+(u\omega_z)$ at $2y_p$ for $R_\theta \simeq 2 \times 10^6$ and $R_\theta \simeq 4 \times 10^6$. For $R_\theta \simeq 2 \times 10^6$, $k^+\Lambda^+(u\omega_z)$ in figure 27(*C*) is different from that at $y_p/2$, with little or no wavenumber range of negative correlation. In contrast, the $k^+\Lambda^+(u\omega_z)$ data in figure 27(*D*) continue to show negative correlations at low wavenumbers.

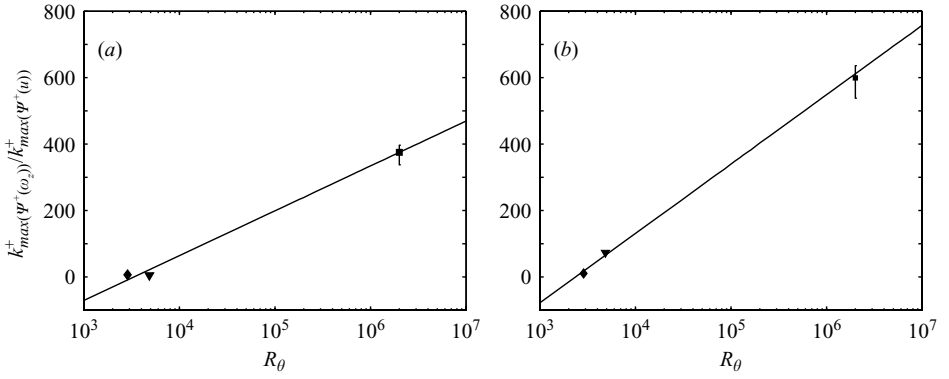

FIGURE 28. Variation in $k^+_{max(\Psi^+(\omega_z))}/k^+_{max(\Psi^+(\omega_u))}$ as a function of R_θ. The symbols are defined in table 3. (*a*) Variation at $y_p/2$. The curve-fit shown is $k^+_{max(\Psi^+(\omega_z))}/k^+_{max(\Psi^+(u))} = 135.0 \log R_\theta - 475.8$. (*b*) Variation at $2y_p$. The curve-fit shown is $k^+_{max(\Psi^+(\omega_z))}/k^+_{max(\Psi^+(u))} = 208.8 \log R_\theta - 704.3$.

Similarly to the analysis in § 3.4.2, the wavenumbers at which the premultiplied power spectra indicate peaks were obtained for all the smooth-wall data; $k^+_{max(\Psi^+(u))}$ is the inner-normalized wavenumber at which $\Psi^+(u)$ peaks and $k^+_{max(\Psi^+(\omega_z))}$ is the inner-normalized wavenumber at which $\Psi^+(\omega_z)$ peaks. The plot of the ratio of these two wavenumbers versus R_θ is shown in figure 28. There is a significant scale separation for the $R_\theta \simeq 2 \times 10^6$ data at $y_p/2$, as shown in figure 28(*a*). This observation is different from that for the power spectra of v and ω_z shown in figure 18(*a*). There is an increase in scale separation at $2y_p$. This increase is, however, less than an order of magnitude. The variations of $k^+_{max(\Psi^+(\omega_z))}/k^+_{max(\Psi^+(u))}$ for low-R_θ smooth-wall and high-R_θ relatively-smooth-wall data are approximately logarithmic. Again, more intermediate R_θ data are required to clarify these trends.

4. Discussion

4.1. *Cospectral properties under increasing scale separation*

The present measurements have revealed a number of specific results, and these are succinctly listed and discussed in the conclusions section below. As indicated in the introduction, however, an over-arching motivation for this study was to understand better the effects of scale separation on the transport mechanisms of wall turbulence. The present approach has been to explore these mechanisms through the study of the velocity–vorticity products associated with (1.4) and (1.6). In this regard it is useful to reiterate briefly and then discuss further the attributes and relevance of this approach to studying scale-separation effects.

As explained in §§ 3.4.2, 3.5.2 and 3.6.2, the respective properties of velocity and vorticity spectra embody naturally instructive attributes with regard to assessing the effects of scale separation. Specifically, with increasing Reynolds number the peaks of the premultiplied velocity power spectra move, at varying rates depending on the component, to increasingly low wavenumbers relative to the peaks in the premultiplied vorticity power spectra. Through this effect, the premultiplied power spectral densities inherently display the influences of scale separation.

According to (1.4), however, it is also true that the relevant velocity and vorticity components must combine to generate a non-zero correlation if, for example, the Reynolds stress-gradient term in (1.1) is to effect a time rate of change of mean

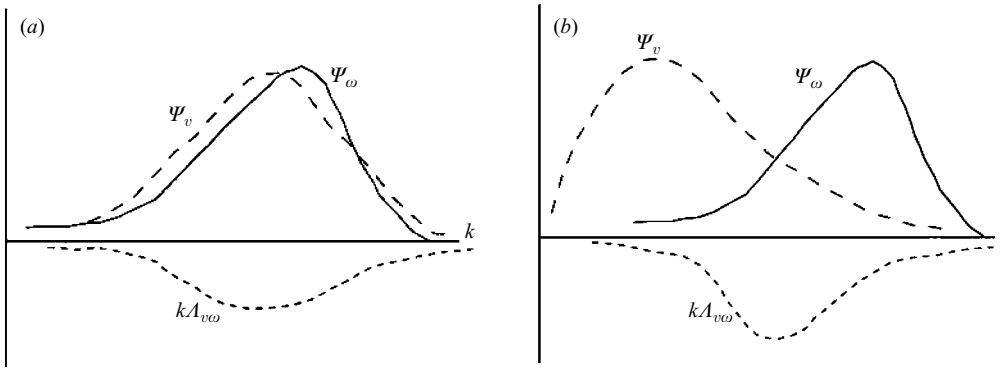

FIGURE 29. View of how increasing scale separation (associated with increasing Reynolds number) was initially anticipated to be reflected in the velocity–vorticity spectra and cospectra. Under this view the cospectral peak remains centred on the overlapping region of the participating velocity- and vorticity-component spectra at all Reynolds numbers. (*a*) Low Reynolds number, (*b*) high Reynolds number.

momentum. Given that the integral of the cospectrum is the covariance, the weighting of the area under the cospectral curve, relative to the weighting of the individual velocity and vorticity spectra, provides a rather direct way of exposing how Reynolds-number-induced scale separation influences the mean transport. In this regard, one rational expectation relating to the correlation might be that the relevant velocity and vorticity components will interact most significantly over the range of wavenumbers common to both spectra. Model spectra depicting such a situation are shown in figures 29(*a*) and 29(*b*) for large and small scale separation, respectively. As depicted, the peaks in the contributing velocity and vorticity spectra move to disparate wavenumbers, while the non-zero portion of the cospectrum remains centred on the overlapping portions of the individual spectra. At low Reynolds number there is minimal scale separation between the velocity and vorticity fields. Under the model picture shown in figure 29(*a*) the overlapping portion of these spectra is significant at low Reynolds number, and thus from these data alone one cannot reliably associate the cospectral peak with the region of spectral overlap. At high Reynolds number, owing to significant scale separation this association between the region of spectral overlap and the predominant contributions to the cospectra becomes apparent.

While the influences of scale separation indicated in figure 29(*a*) are consistent with the notion that similar-wavenumber motions will interact most vigorously, the evolution of the spectra with Reynolds number depicted in this figure is generally not consistent with the present findings. As indicated by figures 16, 17, 22, 26 and 27, the effects of scale separation, appear most distinctly, as illustrated further in figure 30. Specifically, when there is significant scale separation the cospectrum generally does not peak in a range of intermediate wavenumbers common to the velocity and vorticity spectra but rather has separate maxima near to those in the respective velocity and vorticity spectra. These observations are taken to indicate that there is a 'scale selection' that occurs at wavenumbers near the peaks of the participating velocity and vorticity components. Effectively, for the high-wavenumber cospectral peak, high-amplitude vorticity-field fluctuations interact with relatively-small-amplitude velocity-field fluctuations (i.e. they select the velocity-field scales local to the Ψ_ω peak) to produce a considerable contribution to the overall correlation. Similarly, at low wavenumbers the roles are reversed and there is a velocity-field selection of the available low-amplitude vorticity-field fluctuations near the Ψ_V peak.

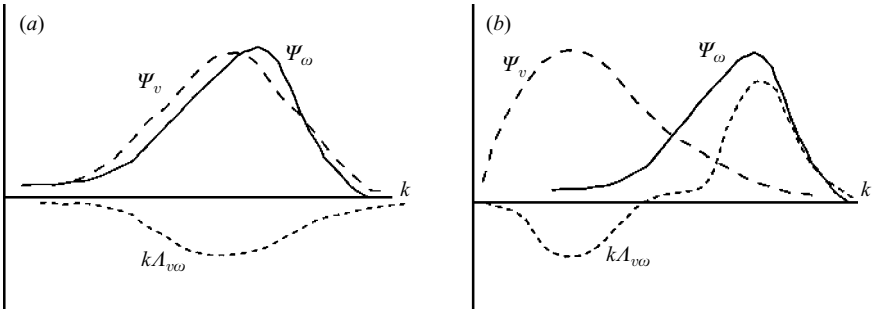

FIGURE 30. Illustration of how increasing scale separation is most generically reflected in the velocity and vorticity spectra and cospectra. The actual observations indicate that the cospectral peaks nominally track the individual spectral peaks of the corresponding velocity and vorticity components. (*a*) Low Reynolds number, (*b*) high Reynolds number.

4.2. *Physical interpretations*

A broadly prevalent notion to emerge from turbulent-structure studies is that coherent-motion dynamics account for a disproportionate contribution to the overall transport of momentum. In this regard, spatially compact vortical motions provide an appropriate context in which to interpret, at least partially, the present results. As depicted in figure 30, the high-wavenumber peak in the velocity–vorticity cospectrum tends to correlate strongly with the maximum in the vorticity spectrum. The characteristic interaction here is taken to be that between a high-intensity patch of the vorticity field and a relatively-low-intensity velocity fluctuation. In this case the contribution to $\Lambda_{V\omega}$ comes from velocity–vorticity interactions local to spatially concentrated patches of advecting vorticity (i.e. local to an advecting vortical motion). Conversely, the characteristic interaction underlying the low-wavenumber peak in the cospectrum is that between a high-amplitude velocity fluctuation and a relatively-low-intensity vorticity fluctuation. The physical interpretation in this regard builds largely upon the previous observations of Adrian and his coworkers; see below. In this case, the velocity-field interaction is with a low-wavenumber vortical motion that has association with the large-scale spacing of smaller-scale vortical motions. This is depicted in figure 31, which is in large part a schematic interpretation of the instantaneous particle image velocimetry (PIV) observations of Meinhart & Adrian (1995).

As might be expected from the relatively large spatial scales involved, wall-layer flow-field quantifications associated with phenomena of the type represented in figure 31 are scarce and, to date, none have explored explicitly the velocity–vorticity-field interactions relevant to (1.2). Recent PIV-based studies do, however, provide insight into how such interactions might be realized. In fact, the findings of Meinhart & Adrian (1995), schematically depicted in figure 31, revealed the existence of large-scale zones of nearly constant axial momentum that are segregated by relatively narrow 'fissures' of highly vortical flow. (Note that these localized highly vortical regions will individually undergo the high-intensity interactions noted above.) Owing to the fact that adjacent zones are of differing momentum (i.e. an increment in momentum is sustained across the vortical fissures), it is conjectured that a low-wavenumber but small-amplitude contribution to the vorticity field is produced when such a spatial structure advects past a stationary probe. Thus, in this way the large-scale organization of small-scale highly vortical motions generates low-intensity low-wavenumber vortical motions that correlate with the spatially coincident

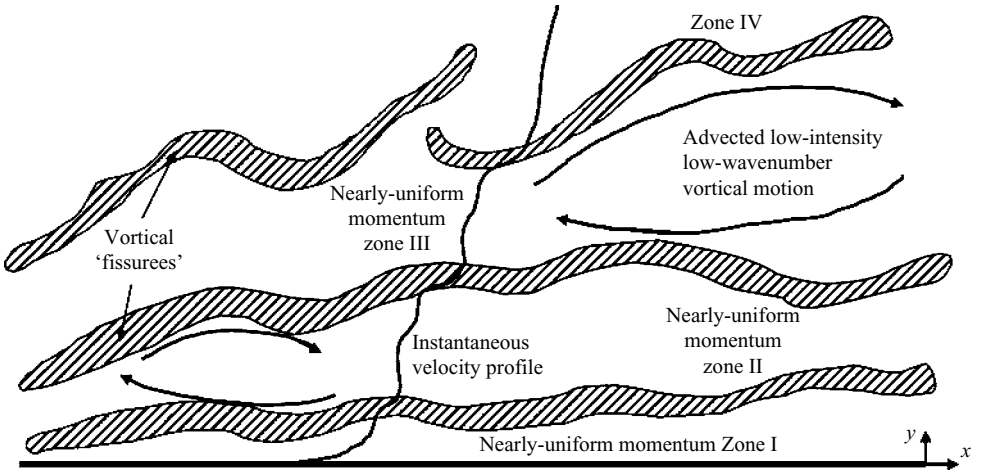

FIGURE 31. Schematic depiction of a large-scale organization of locally concentrated vorticity that could lead to the observed low-wavenumber peak in the velocity–vorticity cospectra. The flow is from left to right with the sense of the mean vorticity into the page. The central features of this depiction are zones of approximately uniform momentum intermittently segregated by narrow fissures of highly vortical flow, as first observed by Meinhart & Adrian (1995). Mounting evidence indicates that this physical picture is established in connection with the hierarchical formation of hairpin-like vortex packets (Meinhart & Adrian 1995; Adrian *et al.* 2000; Hutchins & Marusic 2006).

high-intensity low-wavenumber velocity-field perturbations associated with the uniform momentum zone itself.

Indeed, perhaps the most significant result to come out of recent PIV-based studies is the recognition that wall-layer hairpin-like vortices self-organize into packets and that these packets largely constitute the vortical 'skeleton' that supports the much-larger-scale zones of uniform momentum (Adrian, Meinhart & Tomkins 2000; Ganapathisubramani, Longmire & Marusic 2003). This hypothesized mechanism, by which transport at high wavenumbers generates and maintains low-wavenumber phenomena, has similarities to that observed and theoretically verified in relation to the evolution of passive scalar spectra in pipe-flow mixing (Kerstein & McMurtry 1994; Guilkey *et al.* 1997). In the present case, however, the variables are dynamically active, and thus this mechanism illustrates more broadly how interactions across disparate wavenumbers might be dynamically significant.

The physical picture just described also has noteworthy and self-consistent connections with behaviours anticipated to occur with increasing Reynolds number as well as with increasing distance from the wall at fixed Reynolds number. The first is the expectation that the low-wavenumber cospectral peak of the type observed will emerge only after a sufficient scale separation is established between the participating velocity and vorticity components. (Note that this appears to depend predominantly on the appearance of an increasingly low-wavenumber peak in the velocity component; see below.) Physically, this would only be expected to occur after a sufficient hierarchy of uniform momentum zones (and/or vortex packets) has been established. An increasing number of larger-scale hierarchy members is a central observation relating to the effect of an increase in Reynolds number and/or distance from the wall at fixed Reynolds number (Adrian *et al.* 2000). Figures 18 and 28 quantify this effect. The second relates to the primary attribute of a boundary layer as a region

where viscous effects, though never entirely negligible, occupy a diminishingly smaller fraction of the flow domain with increasing Reynolds number. This attribute is captured in the instantaneous structure of the present model through viscous effects remaining important in the vortical fissures that segregate the uniform momentum zones and thus are responsible for the momentum increment from zone to zone and the associated (hypothesized) low-wavenumber contribution to the vorticity field. With increasing Reynolds number the present physical model predicts that these vortical fissures should occupy a decreasingly smaller fraction of the overall volume within the boundary layer. The nominal invariance of the vorticity spectra under Taylor normalization supports this notion.

While the above discussion provides a description of how the different scales of motion in the velocity and vorticity fields might interact to generate the features observed in the cospectra, the specific interactions between the velocity and vorticity components and their associated dynamical significance are far from being well understood. Generically, however, it is rational to expect that during the spatiotemporal evolution of any given vortical motion the linear momentum in the boundary layer will either increase or decrease. The average of these interactions at any given distance from the wall then leads to the net source or sink nature of the Reynolds-stress gradient as it pertains to the time rate of change of the mean momentum; see (1.5). In this context, the coherent vortical-motion dynamics are effectively reduced to the question whether the result of the interaction imparts or extracts linear momentum. For example, the average interaction for $y < y_p$ is source-like, i.e. $-\partial\overline{uv}/\partial y$ is positive. Similarly, because they predominantly occur in the region $y > y_p$, a large subset of the interactions depicted in figure 31 are anticipated to have a net sink-like effect.

4.3. *Some comments on combined effects of roughness and Reynolds number*

The combined effects of high Reynolds number and significant wall roughness are inherent to a number of the experiments presented herein. Thus, while far from constituting a comprehensive study, some of the present observations are worth referencing to Townsend's similarity hypothesis (Townsend 1976), which, succinctly, states that outside the roughness sublayer the properties of the turbulence become independent of the roughness, as well as recent laboratory studies of rough-wall flows. Specifically, the results of Krogstad *et al.* (1992) for boundary layers over periodic bars and/or meshes do not support Townsend's hypothesis since these authors discerned roughness effects in velocity-fluctuation statistics (especially in the v-component) well outside the roughness sublayer. Conversely, the u and v statistical profiles of Flack *et al.* (2005) for boundary layers over fully rough ($k_s^+ > 100$) sandgrain roughness strongly support Townsend's hypothesis by exhibiting invariance outside the roughness sublayer ($\gtrsim 5k_s$) under inner normalization when plotted versus y/δ. In connection with this, Flack *et al.* (2005) qualified these observations with the proviso that $\delta/k_s > 40$, which, of course, is effectively a statement about scale separation. Even more recently, Bakken *et al.* (2005) presented results from a symmetrically roughened channel (again over bars and meshes) and showed that the results are largely in accord with Townsend's similarity hypothesis. From these results, they surmised that an asymmetry of boundary conditions is the source of previous observations that are contrary to Townsend's hypothesis.

Regarding the present measurements, it is important to note that the roughness at the SLTEST site is much more like a randomly distributed, sandgrain type roughness than regular bars or meshes. Relative to sandgrain roughness, however, the playa

naturally contains a considerably broader spectrum of roughness amplitudes and wavelengths. It is also relevant to recognize that, unlike the lower-Reynolds-number studies of Krogstad *et al.* (1992), Flack *et al.* (2005) and Bakken *et al.* (2005), positions outside the roughness sublayer of even the present $k_s^+ = 500$ flow are still very deep within the inner layer (i.e. δ/k_s for this flow is about 2000). With these considerations in mind, the present results indicate that outside the roughness sublayer the u'^+ profile exhibits a clear Reynolds-number dependence while at most only a mild sensitivity to roughness. Conversely, the v'^+ profile is invariant with Reynolds number (above a low-Reynolds-number regime) but exhibits a discernible sensitivity to roughness. Lastly, neither the ${\omega_y}'^+$ nor the ${\omega_z}'^+$ data reveal any discernible effect of roughness or Reynolds number under inner normalization.

The observed sensitivities to surface roughness are difficult to attribute to the asymmetric-boundary-condition effect proposed by Bakken *et al.* (2005). Specifically, measurements over the past decade indicate that wall-layer-turbulence statistics at the SLTEST site exhibit remarkable consistency from experiment to experiment. Of course, the 'freestream' flow for the atmospheric surface layer is the so-called mixed layer. The horizontal mean flow in the mixed layer is near to being uniform, but the turbulence is non-negligible. From experiment to experiment, however, one can be virtually assured that this freestream condition varies. Therefore, given that this variable-freestream condition does not cause detectable effects on the near-surface turbulence statistics, it is difficult to imagine how roughness located at a remote opposing wall might remove such an effect. However, the present sensitivities to a distributed type of roughness are also counter to the observations of Flack *et al.* (2005) over sandgrain roughness. One plausible means of reconciling this apparent disagreement is via the notion that the roughness problem is Reynolds-number dependent. More specifically, there may be roughness regimes for $k_s^+ \gg 1$ and $k_s/\delta \ll 1$ that, by definition, only become apparent under the condition of large scale separation. In any case, the present observations that the vorticity intensities are insensitive to roughness (and Reynolds number) while the velocity intensities are not, provide support to the notion that the characteristic scale of the motion affects their sensitivity to roughness.

4.4. *Additional observations*

Regarding the above interpretations, a few additional comments and observations are worth noting.

The spectral analyses clearly reveal that the effects of scale separation occur at different rates with increasing Reynolds number depending on the velocity–vorticity-component combinations involved. For example, the spectral peaks of $\Psi(u)$ and $\Psi(\omega_z)$ are separated by about a decade in wavenumber even at $\delta^+ \simeq 1500$, while at the same Reynolds number the spectral peaks of $\Psi(v)$ and $\Psi(\omega_z)$ are nearly coincident. The rate of scale separation for $\Psi(w)$ and $\Psi(\omega_y)$ appears to be intermediate to these two extremes. Thus, the effects of scale separation with increasing Reynolds number are realized at different rates for the two velocity–vorticity products contributing to $-\partial\overline{uv}/\partial y$. Overall, the present data also show that the variability in the peaks of the different velocity components (as opposed to the vorticity components) is the most significant factor underlying the degree of scale separation. Of course, an increasing separation in the peaks of the velocity and vorticity spectra occurs both with increasing Reynolds number and increasing distance from the wall.

These observations also have relevance to an important question: how high must the Reynolds number be (say in a well-resolved laboratory experiment or DNS)

before the effects of scale separation are reliably revealed? A clear result exemplified, for example, by the study of DeGraaff & Eaton (2000) is useful in this regard. Specifically, because dependences often occur approximately logarithmically with Reynolds number, well-resolved experiments should look for about one decade in variation in the relevant parameter before the dependences can be said to be reliably revealed. In the present case, the most stringent requirements relate to $\Psi(v)$ and $\Psi(\omega_z)$. As just mentioned, these two spectra are nearly indistinguishable at $\delta^+ \simeq 1500\ y_p/2$. At $\delta^+ \approx 10^6$, however, the spectral peaks of $\Psi(v)$ and $\Psi(\omega_z)$ are separated by more than a decade in wavenumber at $y_p/2$. Assuming a nominally logarithmic variation in the wavenumber increment between these two peaks with Reynolds number, then a one-decade separation in the peaks of $\Psi(v)$ and $\Psi(\omega_z)$ will be attained at $\delta^+ \approx 39\,000$. This estimate applies to scale-separation effects on the dynamics; see (1.4). Interestingly, significant scale-separation effects pertinent to the kinetic-energy gradient given in (1.6) are realized at considerably lower Reynolds numbers.

An interesting broader observation relates to the types of vortical motions and flow-field interactions that one might expect to be most dynamically significant. Over the past decade or so, considerable effort within the turbulence community has been devoted toward analysis methods that define and identify vortices. A pervasive underlying theme in this regard has been a bias toward the study of swirling-type motions, i.e. those that in cross-section and for a selected advection velocity of the observer have a nominally closed, nominally circular, streamline pattern. The underlying focus of the present study is a distinctly different approach. Specifically, the present method seeks to identify those localized distributions of vorticity (and their interactions with the velocity field) that affect a time rate of change of momentum. Notable features of this approach are that the motions studied are the actual field variables and that their interactions can be directly related to both the instantaneous and time-averaged forms of the governing dynamical equations. (As far as the authors are aware, there are no rigorously developed equations that solely and specifically describe the dynamics of coherent vortices.) When viewed in this manner, there is no *a priori* justification for isolating and specifically studying swirling-type vortical motions. That is, by (1.4), turbulent-stress-gradient generation requires only that specific velocity and vorticity components are correlated.

5. Conclusions

The velocity–vorticity products $v\omega_z$ and $w\omega_y$, contributing to the wall-normal gradient of the Reynolds shear stress, and $u\omega_z$, contributing to the wall-normal gradient of the turbulent kinetic energy, were analyzed in this study. The flow fields considered were low-R_θ smooth-wall and very-high-R_θ relatively-smooth- and rough-wall turbulent boundary layers.

The conclusions derived from this study are as follows.

(*a*) The inner-normalized streamwise velocity intensity is relatively sensitive to increasing R_θ. This statistic is considerably less sensitive to increasing wall roughness. Conversely, the inner-normalized wall-normal velocity intensity is insensitive to increasing R_θ (above, say, $R_\theta \simeq 2000$), but displays a detectable sensitivity to increasing wall roughness. The inner-normalized spanwise velocity intensity exhibits an R_θ-dependence similar to that exhibited by u'^+. The inner-normalized wall-normal vorticity intensity appears to be largely independent of both R_θ and wall roughness. Except near the edge of the viscous sublayer, the inner-normalized spanwise vorticity intensity is also insensitive to both R_θ and wall roughness.

(*b*) The $\overline{v\omega_z}^+$ and especially the $\rho_{v\omega_z}$ profiles show clear R_θ and wall-roughness dependences. The r.m.s. fluctuations in $(v\omega_z)^+$ appear to be largely insensitive to both R_θ and wall roughness. The cospectrum of v and ω_z is dependent on R_θ, wall roughness and wall-normal position. Its behaviour is summarized as follows.

(i) The characteristic motions underlying the high-R_θ smooth-wall $v\omega_z$ cospectrum for $y > y_p$ are of larger scale than at $y_p/2$. This scale is nominally given by the wavenumber of the peak in $\Psi(v)$.

(ii) Owing to a lack of scale separation, the characteristic scale of the motions contributing to the $v\omega_z$ cospectrum for the smooth-wall $y < y_p$ low-R_θ flow is relatively large when compared with the data at high-R_θ. The characteristic scales contributing to this cospectrum in the smooth-wall $y < y_p$ high-R_θ flow are of the order of the Taylor wavenumber.

(iii) The correlation between the low wavenumbers in v and ω_z is positive for smooth-wall high-R_θ turbulent boundary layers. This correlation is negative for the low-wavenumber portion of the cospectrum in the rough-wall high-R_θ flows.

(*c*) For the present high-R_θ rough-wall turbulent boundary layers, correlations between the w and ω_y motions are negative for $y \lesssim y_p$ and positive for $y \gtrsim y_p$. This correlates well with the change in sign of the $-\partial\overline{uv}/\partial y$ profile. Irrespective of the wall-normal location, the characteristic scales of the $w\omega_y$ motions in the high-R_θ rough-wall flow are of the order of the Taylor microscale. There are, however, non-negligible correlations between the larger-scale ω_y and w motions. The amplitudes of these correlations are, however, smaller than those near the Taylor wavenumber.

(*d*) The correlation between u and ω_z shows very little R_θ dependence. This correlation is also relatively insensitive to wall roughness. The characteristic scales of the u and ω_z correlations are considerably different from those of the $\boldsymbol{v}$ and ω_z correlations. There is a significant scale separation (even at low-R_θ) between the peaks in the u and ω_z power spectra. Therefore, there are noticeable correlations between low-wavenumber small-amplitude ω_z motions and large-amplitude u motions. In addition, there are correlations between high-wavenumber large-amplitude ω_z motions and low-amplitude u motions. Both these combinations contribute significantly to the u–ω_z cospectrum.

This work was supported by the National Science Foundation and the Office of Naval Research under grants CTS-0120061 (grant monitor Dr Michael W. Plesniak) and N00014-00-1-0753 (grant monitor Dr Ronald D. Joslin), respectively.

REFERENCES

Adrian, R. J., Meinhart, C. D. & Tomkins, C. D. 2000 Vortex organization in the outer region of the turbulent boundary layer. *J. Fluid Mech.* **422**, 1–54.

Bakken, O. M., Krogstad, P. A., Ashrafian, A. & Andersson, H. I. 2005 Reynolds number effects in the outer layer of the turbulent flow in channel with rough walls. *Phys. Fluids* **17**, (065101–1)–(065101–16).

Balint, J., Vukoslavcevic, P. & Wallace, J. M. 1987 A study of vortical structure of the turbulent boundary layer. In *Advances in Turbulence* (ed. G. Comte-Bellot & J. Mathieu), pp. 456–464. Springer.

Balint, J., Wallace, J. M. & Vukoslavcevic, P. 1991 The velocity and vorticity vector fields of a turbulent boundary layer. Part 2. Statistical properties. *J. Fluid Mech.* **228**, 53–86.

Bendat, J. S. & Piersol, A. G. 1986 *Random Data: Analysis and Measurement Procedures*. Wiley.

Crawford, C. H. & Karniadakis, G. E. 1997 Reynolds stress analysis of emhd-controlled wall turbulence. part i. streamwise forcing. *Phys. Fluids* **9**, 788–806.

DeGraaff, D. B. & Eaton, J. K. 2000 Reynolds-number scaling of flat-plate turbulent boundary layer. *J. Fluid Mech.* **422**, 319–346.

Falco, R. E. 1977 Coherent motions in the outer region of turbulent boundary layers. *Phys. Fluids* **20**, S124–S132.

Falco, R. E. 1983 New results, a review and synthesis of the mechanism of turbulence production in boundary layers and its modification. *Paper AIAA* 83-0377.

Falco, R. E. 1991 A coherent structure model of the turbulent boundary layer and its ability to predict Reynolds number dependence. *J. Inform. Phil. Trans.: Phys. Sci. Engng* **336**, 103–129.

Fernholz, H. H. & Finley, P. J. 1996 The incompressible zero-pressure-gradient turbulent boundary layer: an assessment of the data. *Prog. Aerospace Sci.* **32**, 245–311.

Flack, K. A., Schultz, M. P. & Shapiro, T. A. 2005 Experimental support for Townsend's Reynolds number similarity hypothesis on rough walls. *Phys. Fluids* **17**, 035102.

Folz, A. B. 1997 An experimental study of the near-surface turbulence in the atmospheric boundary layer. PhD thesis, University of Maryland at College Park.

Foss, J. F. 1994 The pulse width modulated-constant temperature anemometer. *Expl Therm. Fluid Sci.* **8**, 260–270.

Foss, J. F., Bohl, D. G. & Hicks, T. J. 1996 The pulse width modulated-constant temperature anemometer. *Meas. Sci. Technol.* **7**, 1388–1395.

Gad el Hak, M. & Bandyopadyay, P. R. 1994 Reynolds number effects in the wall-bounded turbulent flows. *Appl. Mech. Rev.* **47**, 307–365.

Ganapathisubramani, B., Longmire, E. & Marusic, I. 2003 Structural features of turbulent flow over smooth and rough boundaries. *J. Fluid Mech.* **478**, 35–46.

Guilkey, J. E., Kerstein, A. R., McMurtry, P. A. & Klewicki, J. C. 1997 Mixing mechanisms in turbulent pipe flow. *Phys. Fluids* **9**, 717.

Hinze, J. O. 1975 *Turbulence*. McGraw-Hill.

Honkan, A. & Andreopoulos, Y. 1997 Vorticity, strain-rate and dissipation characteristics in the near-wall region of turbulent boundary layers. *J. Fluid Mech.* **350**, 29–96.

Hutchins, N. & Marusic, I. 2006 Investigation of the log region structure in wall bounded turbulence. *AIAA Paper* 2006-325.

Kerstein, A. R. & McMurtry, P. A. 1994 Low-wave-number statistics of randomly advected passive scalars. *Phys Rev* E **50**, 2057–2063.

Klewicki, J. C. 1989*a* On the interaction between the inner and outer region motions in turbulent boundary layers. PhD thesis, Michigan State University.

Klewicki, J. C. 1989*b* Velocity-vorticity correlations related to the gradients of the Reynolds stress in parallel turbulent wall flows. *Phys. Fluids* A **1**, 1285–1288.

Klewicki, J. C. & Falco, R. E. 1990 On accurately measuring statistics associated with small-scale structure in turbulent boundary layers using hot-wire probes. *J. Fluid Mech.* **219**, 119–142.

Klewicki, J. C. & Falco, R. E. 1996 Spanwise vorticity structure in turbulent boundary layers. *Intl J. Heat Fluid Flow* **17**, 363–376.

Klewicki, J. C., Falco, R. E. & Foss, J. F. 1992 Some characteristics of the vortical motions in the outer region of the turbulent boundary layers. *Trans. ASME: J. Fluids Engng* **114**, 530–536.

Klewicki, J. C. & Metzger, M. M. 2004 Studies of high Reynolds number turbulence in the atmospheric surface layer over the salt playa of western Utah. In *Proc. IUTAM Symp. on Reynolds Number Scaling in Turbulent Flow, 11–13 September 2002* (ed. A. J. Smits), pp. 45–52. Kluwer.

Klewicki, J. C., Murray, J. A. & Falco, R. E. 1994 Vortical motion contributions to stress transport in turbulent boundary layer. *Phys. Fluids* **6**, 277–286.

Krogstad, P. A., Antonia, R. A. & Browne, L. W. B. 1992 Comparison between rough- and smooth-wall turbulent boundary layers. *J. Fluid Mech.* **245**, 599–617.

Lele, S. K. 1992 Vorticity form of turbulence transport equations. *Phys. Fluids* **4**, 1767–1772.

Marusic, I., Uddin, A. K. M. & Perry, A. E. 1997 Inertial ranges in two-dimensional turbulence. *Phys. Fluids* **9**, 3718–3726.

Meinhart, C. D. & Adrian, R. J. 1995 On the existence of uniform momentum zones in a turbulent boundary layer. *Phys. Fluids* **7**, 694–696.

Metzger, M. M. 2002 Scalar dispersion in high Reynolds number boundary layer. PhD thesis, University of Utah, Salt Lake City, UT.

Metzger, M. M. & Klewicki, J. C. 2001 A comparative study of near-wall turbulence in high and low Reynolds number boundary layers. *Phys. Fluids* **13**, 692–701.

Metzger, M. M., Klewicki, J. C., Bradshaw, K. L. & Sadr, R. 2001 Scaling of near-wall axial turbulent stress in the zero pressure gradient boundary layer. *Phys. Fluids* **13**, 1819–1821.

Morris, S. C. & Foss, J. F. 2004 Non self similar scaling of vorticity in a shear layer. In *Proc. IUTAM Symp. on Reynolds Number Scaling in Turbulent Flow, 11–13 September 2002* (ed. A. J. Smits), pp. 65–70. Kluwer.

Nagib, H. M., Chauhan, K. A. & Monkewitz, P. A. 2005 Scaling of high Reynolds number turbulent boundary layers revisited. *AIAA Paper* 2005–4810.

Ong, L. 1992 Visualization of turbulent flows with simultaneous velocity and vorticity measurements. PhD thesis, University of Maryland.

Perry, A. E. & Chong, M. S. 1982 On the mechanisms of wall turbulence. *J. Fluid Mech.* **119**, 173–217.

Perry, A. E. & Marusic, I. 1995 A wake-model for the turbulent structure of boundary layers. Part 1. Extension of attached eddy hypothesis. *J. Fluid Mech.* **298**, 361–388.

Prandtl, L. 1925 Bericht über untersuchungen zur ausgebildeten turbulenz. *Z. Angew. Math. Mech.* **5**, 136–139.

Priyadarshana, P. A. 2004 Reynolds number influences on turbulent boundary layer momentum transport. PhD thesis, University of Utah, Salt Lake City, UT.

Priyadarshana, P. A. & Klewicki, J. C. 2004*a* Reynolds number scaling of wall layer velocity-vorticity products. In *Proc. IUTAM Symp. on Reynolds Number Scaling in Turbulent Flow, 11–13 September 2002* (ed. A. J. Smits), pp. 117–122. Kluwer.

Priyadarshana, P. A. & Klewicki, J. C. 2004*b* Study of the motions contributing to the Reynolds stress in high and low Reynolds number turbulent boundary layers. *Phys. Fluids* **16**, 4586–4600.

Rajagopalan, S. & Antonia, R. A. 1993 Structure of the velocity field associated with the spanwise vorticity in the wall region of a turbulent boundary layer. *Phys. Fluids* A **5**, 2502–2510.

Robinson, S. K. 1991 Coherent motions in the turbulent boundary layer. *Annu. Rev. Fluid Mech.* **23**, 601–639.

Rovelstad, A. L. 1991 Lagrangian analysis of vorticity transport in a numerically simulated turbulent channel flow. PhD thesis, University of Maryland.

Saddoughi, S. G. & Veeravalli, S. V. 1994 Local isotropy in turbulent boundary layers at high Reynolds number. *J. Fluid Mech.* **268**, 333–372.

Sadr, R. & Klewicki, J. C. 2000 Surface shear stress measurement system for boundary layer flow over a salt playa. *Meas. Sci. Technol.* **11**, 1403–1413.

Shiavi, R. 1999 *Introduction to Applied Statistical Signal Analysis*. Academic.

Smith, C. R., Walker, J. D. A., Haidari, A. H. & Sobrun, U. 1991 On the dynamics of near-wall turbulence. *J. Inform. Phil. Trans.: Phys. Sci. Engng* **336**, 131–175.

Spalart, P. R. 1988 Direct simulation of a turbulent boundary layer up to $R_\theta = 1410$. *J. Fluid Mech.* **187**, 61–98.

Sreenivasan, K. R. 1989 The turbulent boundary layer. In *Frontiers in Experimental Fluid Mechanics* (ed. G. E. Hak), pp. 159–209. Springer.

Tennekes, H. & Lumley, J. L. 1994 *A First Course in Turbulence*. The MIT Press.

Townsend, A. A. 1961 Equilibrium layers and wall turbulence. *J. Fluid Mech.* **11**, 97–120.

Townsend, A. A. 1976 *The Structure of Turbulent Shear Flow*, 2nd edn. Cambridge University Press.

Treat, S. 2006 Velocity-vorticity correlations in a high r_θ turbulent boundary layer. Master's thesis, Michigan State University, East Lansing, MI.

Wallace, J. M. & Foss, J. F. 1995 The measurement of vorticity in turbulent flows. *Annu. Rev. Fluid Mech.* **27**, 469–514.

Wei, T., Fife, P., Klewicki, J. C. & McMurtry, P. A. 2005 Properties of the mean momentum balance in turbulent boundary layer, pipe and channel flows. *J. Fluid Mech.* **522**, 303–327.

Willmarth, W. W. 1975 Structure of turbulent boundary layers. *Adv. Appl. Mech.* **15**, 159–254.

Wu, J., Zhou, Y. & Wu, J. 1996 Reduced stress tensor and dissipation and the transport of lamb vector. *Tech. Rep.* 96-21. Institute for Computer Applications in Science and Engineering, NASA Langley Research Center, Hampton, VA 23681-0001.

Wyngaard, J. C. 1969 Spatial resolution of the vorticity meter and other hot-wire arrays. *J. Sci. Instrum.* **2**, 983–987.